JOURNAL OF GEOPHYSICAL RESEARCH, VOL. 97, NO. D17, PAGES 19,033–19,059, NOVEMBER 30, 1992

Relations Between Surface Conductance and Spectral Vegetation Indices at Intermediate (100 m^2 to 15 km^2) Length Scales

PIERS J. SELLERS

NASA Goddard Space Flight Center, Greenbelt, Maryland

MARK D. HEISER

COLA, Department of Meteorology, University of Maryland, College Park

FORREST G. HALL

NASA Goddard Space Flight Center, Greenbelt, Maryland

The theoretical analysis of Sellers et al. (1992) indicates that the relative response of the unstressed canopy conductance (g_c^*) to changes in incident (nonsaturating) PAR flux (F_0) should be proportional to some spectral vegetation indices (SVI), specifically the simple ratio (SR) vegetation index, for vegetation covers of similar physiology and physiognomy; or $\nabla_F \equiv (\partial g_c^*/\partial F_0) \propto$ SR. This relationship was tested using the First International Satellite Land Surface Climatology Project (ISLSCP) Field Experiment (FIFE) flux station data set (g_c^*) and the FIFE Landsat thematic mapper image data (SVI). The flux station data were used to invert a soil-plant-atmosphere model (the simple biosphere model (SiB) of Sellers et al., 1986) to derive estimates of g_c^* separate from the soil evaporation contribution and corrected for the "stress" effects of vapor pressure deficit and soil moisture deficit. The Landsat imagery was sampled to produce SR vegetation index values for small areas (90 × 90 m) centered on each flux station. The derived ∇_F and SR values were found to be near-linearly related on a site-by-site basis. Differences between sites are thought to be related to the fractional cover of C_3 versus C_4 vegetation so that $\nabla_{S,F} \equiv (\partial \nabla_F/\partial(\mathrm{SR})) \propto V_3$, where V_3 is the fractional cover of C_3 vegetation. The above equations form the basis for a simple biophysically based model of canopy-scale conductance. The model was applied on the flux station scale $(100\ \mathrm{m})^2$ and was also used to calculate fluxes for the entire FIFE site $(15 \times 15\ \mathrm{km})^2$; the latter results were compared with airborne flux measurements. It is demonstrated that because the proposed relationship between ∇_F and SR is near-linear, the calculation of evapotranspiration rates for large areas using this model is effectively scale-invariant.

1. INTRODUCTION

The last decade has seen a great deal of research effort invested in the study of the links between surface biophysical processes, specifically photosynthesis and transpiration, and spectral vegetation indices (SVI). *Asrar et al.* [1984] showed that for a homogeneous wheat canopy the simple ratio (SR) or normalized difference (ND) vegetation indices were near-linearly related to the fraction of the incident photosynthetically active radiation absorbed by the canopy (FPAR; referred to as APAR in many previous papers, including *Sellers* [1985, 1987]). *Monteith* [1977] and *Goward et al.* [1985] reported that the time integral of FPAR, as estimated from surface and satellite SVI measurements, respectively, was near-linearly related to the net primary production (NPP) of the vegetated surface under observation. *Sellers* [1985, 1987], using simple empirical models of leaf photosynthesis and conductance, presented theoretical analyses which indicated that canopy FPAR, the unstressed canopy photosynthetic rate, A_c^*, and the unstressed canopy conductance, g_c^*, should all be near-linearly related to the SR vegetation index under normal agricultural conditions (dark soil background, homogeneous vegetation cover). *Hall et al.* [1990] showed how the second derivative of canopy reflectance with respect to wavelength should be a good indicator of FPAR while also being less prone to interference from variations in soil reflectance.

Sellers et al. [1992] made use of more sophisticated and realistic models of leaf photosynthesis and stomatal function than those described in the works of *Sellers* [1985, 1987]: their reanalysis strongly suggests that the relationships among A_c^*, g_c^*, FPAR, and certain SVI should be more or less scale-independent for vegetation covers of similar physiology and physiognomy. Additionally, the near-linearity between the derivatives of A_c^* and g_c^* with respect to incident PAR and the SVI was even more strongly supported by the results of this more recent study.

The FIFE experiment has provided an incomparable data set with which to test these theories. In this paper we describe how data from many of the FIFE 87 surface flux stations were analyzed to produce estimates of canopy conductance parameters for the areas around the flux station sites, and how data from the Landsat thematic mapper (TM) instrument were used to calculate corresponding SR values. These biophysical and spectral data are compared with each other in the context of the theoretical analyses described above. The results from this exercise are used to calibrate a simple model of the surface energy balance which is partly

Paper number 92JD01096.
0148-0227/92/92JD-01096$05.00

forced by satellite data. The model is then used to calculate surface heat and moisture fluxes over a wide range of scales.

2. Theoretical Background

Sellers et al. [1992] built on the work of *Farquhar et al.* [1980] on leaf photosynthesis, *Ball* [1988] and *Collatz et al.* [1991] on leaf conductance, and *Field and Mooney* [1986] on ecophysiological optimality to construct a model of canopy photosynthesis and conductance. This model was manipulated to give the following relationship among area-averaged canopy biophysical process rates (photosynthesis, conductance), vegetation physiological properties, environmental conditions, and canopy density, and architecture.

$$\begin{pmatrix}\text{canopy}\\ \text{biophysical}\\ \text{rate variable}\end{pmatrix} = \begin{pmatrix}\text{leaf physiology}\\ \text{or}\\ \text{radiation rate limit}\end{pmatrix}\begin{pmatrix}\text{environmental}\\ \text{forcing or}\\ \text{feedback}\end{pmatrix}\begin{pmatrix}\text{canopy PAR}\\ \text{use}\\ \text{parameter}\end{pmatrix}$$

$$A_c = [V_{\max_0}, F_0][B_1, \cdots, B_4]\Pi \quad (1a)$$

$$g_c = [V_{\max_0}, F_0][B_1, \cdots, B_6]\Pi, \quad (1b)$$

where

A_c = canopy photosynthetic rate, μmol m^{-2} s^{-1};
g_c = canopy conductance, m s^{-1};
$V_{\max_0}$ = maximum catalytic capacity of carboxylasing enzyme (Rubisco) in the canopy Sun leaves, μmol m^{-2} s^{-1};
F_0 = incident flux of PAR, W m^{-2};
Π = canopy PAR use parameter;
$= \overline{\text{FPAR}}/\bar{k}_\pi$;
$\overline{\text{FPAR}}$ = time-mean (radiation-weighted) fraction of PAR absorbed by the canopy;
$\bar{k}_\pi$ = time-mean (radiation-weighted) extinction coefficient for PAR;
$B_1, \cdots, B_6$ = environmental forcing or feedback factors;
$(\cdots)$ = "multivalued function of".

The three terms on the right-hand side of (1) are discussed in turn below.

Leaf physiology or radiation rate limit ($V_{\max_0}, F_0$). $V_{\max_0}$ is the physiological limit to leaf photosynthesis for the ensemble of leaves at the top of the canopy exposed to the incident insolation; it determines the maximum photosynthetic rate of these leaves under stress-free (stress is defined below), light-saturated conditions and is roughly proportional to the amount of Rubisco (carboxylasing enzyme) or nitrogen in the leaf. Inferior leaves in the canopy have lower nitrogen contents, see *Schimel et al.* [1991], *Kittel et al.* [1990], and *Field and Mooney* [1986], so that the profile of $V_{\max}$ down through the canopy follows the attenuation of the time-mean (radiation-weighted) PAR flux. This arrangement is optimally efficient in terms of maximizing canopy photosynthetic capacity for a given amount of canopy nitrogen. It also means that all the leaves in the canopy light saturate at the same incident PAR flux (F_0) above the canopy, see *Sellers et al.* [1992]. Below this, canopy saturation values of F_0, (F_0^{sat}), A_c, and g_c are more or less linear functions of F_0.

The environmental forcing or feedback factors (B_1 through B_6). These cover the effects of the ambient atmospheric temperature, vapor pressure deficit, turbulent transfer conditions, and CO_2 concentration on photosynthesis and transpiration; the list can be expanded to include the effect of soil moisture stress. These factors are discussed in full by *Sellers et al.* [1992] and are reviewed briefly later on in this paper.

The canopy PAR use parameter (Π). This is the third term in (1) and is the principal focus of this paper. It is given by the radiation-weighted, time-mean value of FPAR divided by the extinction coefficient for PAR within the canopy, $\bar{k}_\pi$.

The photosynthesis-conductance model for a single leaf as proposed by *Ball* [1988] and *Collatz et al.* [1991] corresponds to (1) except that in the single-leaf model the canopy PAR use parameter Π is replaced by unity. The parameter Π is the bulk canopy term that results from the integration of this leaf-scale physiological model over the depth of the canopy, see *Sellers et al.* [1992]. For a closed canopy, $\overline{\text{FPAR}} \to 1$, and Π will hold a value between 1 and 2, depending on leaf inclination. The value of Π is arrived at by integrating the function that defines the attenuation of PAR within the canopy over the depth of the canopy; thus

$$\Pi = \int_0^{L_T} V_c \overline{f(L)}\, dL, \quad (2)$$

where

$F = F_0 f(L)$;
F = mean PAR flux at leaf area index L within the canopy, W m^{-2};
F_0 = PAR flux incident on the canopy, W m^{-2};
$f(L)$ = PAR attenuation function;
L = cumulative local leaf area index;
V_c = canopy cover fraction;
L_T = total local canopy leaf area index.

An exponential extinction model [*Goudriaan*, 1977; *Sellers*, 1985, 1987; *Sellers et al.*, 1992] is used to describe the attenuation of PAR as a function of cumulative leaf area index.

$$f(L) = e^{-k_\pi L}, \quad (3)$$

so that when a time-mean version of (3) is inserted into (2) and solved, we have

$$\Pi = \frac{V_c(1 - e^{-\bar{k}_\pi L_T})}{\bar{k}_\pi} \quad (4a)$$

$$\approx \frac{\overline{\text{FPAR}}}{\bar{k}_\pi}, \quad (4b)$$

where the overbar symbol in (4) refers to a radiation-weighted time-mean value; $\bar{k}_\pi$, the time-mean extinction coefficient for PAR in the canopy, is obtained from a semiempirical function [*Goudriaan*, 1977, equation (2.40)].

$$k_\pi = \frac{G(\mu)}{\mu}(1 - \omega_\pi)^{1/2}, \quad (5)$$

where

$G(\mu)$ = projected area of leaf in direction of PAR flux, μ;
μ = cosine of PAR flux zenith angle,
$\approx$ cosine of solar zenith angle;
ω_π = leaf scattering coefficient for PAR flux,
≈ 0.2.

The value of Π varies from zero (if either V_c or L_T are zero) to around two for a dense homogeneous vegetation cover. In the latter case, the area-averaged canopy biophysical rate (A_c or g_c) would thus be roughly twice the mean leaf scale biophysical rate associated with the ensemble of leaves at the top of the canopy, according to (1). It is this parameter Π which is amenable to remote sensing. Interestingly, the analysis of *Sellers et al.* [1992] indicates that while A_c and g_c are linearly related to Π and FPAR in (1), they are neither linearly nor uniquely related to L_T for a given vegetation physiology ($V_{\max_0}$).

Sellers [1985, 1987] explored the relationship among the SVIs, FPAR, and canopy biophysical processes. A two-stream approximation model was used to explore the effects of variations in the total leaf area index, L_T, on FPAR and reflectance, for the case of a homogeneous, plane parallel canopy. With a dark soil background and a green canopy it was shown that

$$\mathrm{SR} \equiv \frac{\rho_N}{\rho_v} \propto \mathrm{FPAR}, \tag{6}$$

for

$$\frac{\partial \rho_V}{\partial L_T} \ll \frac{\partial \rho_N}{\partial L_T}$$

where ρ_N, ρ_V are near-infrared, visible reflectance, respectively (sensor-dependent).

Equation (6) should hold for a green uniform canopy overlying a dark soil background such that the soil reflectance in the visible region is roughly equal to that of an infinitely deep canopy. (The effects of nongreen material in the canopy and different soil backgrounds on the relationships between SVIs and FPAR are explored by *Sellers* [1985, 1987], *Choudhury* [1987], and *Hall et al.* [1990]). This condition, which is more or less valid for herbaceous vegetation growing on dark organic soils, means that the observed visible reflectance shows relatively small variations with changes in leaf area index, as specified by the inequality under (6), and so SR is near-linearly related to changes in the near-infrared reflectance, ρ_N. The dependence of ρ_N on total leaf area index, as given by the two-stream approximation model described by *Sellers* [1985, 1987], can then be summarized by

$$\mathrm{SR} \propto \rho_N \propto V_c(1 - e^{-2h_N L_T}), \tag{7}$$

where h_N is extinction coefficient for diffuse near-infrared radiation and is equal to $(1 - \omega_N)^{1/2}$.

Inspection of (4), (6), and (7) shows that FPAR will be proportional to SR if $2h_N L_T = k_\pi L_T$, or

$$(1 - \omega_N) = \left[\frac{G(\mu)}{2\mu}\right]^2 (1 - \omega_\pi). \tag{8}$$

In (8) we must be careful to specify the wavelength intervals which define ω_N and ω_π. In practice, these are functions of the spectral response functions of the satellite or airborne sensor in question, see *Sellers* [1987, equation (33)]. The Landsat thematic mapper channels TM-3 (visible) and TM-4 (near-infrared) have spectral response functions which provide estimates of $\omega_\pi = 0.12$–0.18 and $\omega_N \simeq 0.96$ for green Konza grass vegetation, according to E. A. Walter-Shea (personal communication, 1992). These values approximately satisfy (8) for a spherical leaf angle distribution, $G(\mu) = 0.5$, and intermediate solar zenith angles, $\mu \simeq 0.5$. Also, it should be noted that the analyses discussed above considered only the hemispherically integrated surface reflectances as calculated by a two-stream model, while in practice, SVIs are derived from satellite radiances. The effects of viewing and illumination geometry, atmospheric scattering, and surface anisotropy on the observed radiances are discussed in a few papers in the Surface Radiances and Biology section of this issue. For now, we will assume that the radiometrically rectified Landsat SR product [see *Hall et al.*, 1991] approximately conforms to the simple relationships described above; this assumption is supported by results presented by *Hall et al.* [1990].

The analysis of *Sellers* [1985, 1987], summarized above, was focused on the case of horizontally continuous canopies, that is, $V_c = 1$, of varying (optical) depth. *Hall et al.* [1990] considered an alternative scenario where the vegetation cover was assumed to consist of dense units which occupy varying cover fractions of the landscape (or the sensor field of view), that is, a vegetation cover of varying horizontal density such as coniferous forests or desert shrubs. *Hall et al.* [1990] showed that for this case also, some SVIs would be near-linearly related to FPAR.

Sellers et al. [1992] reviewed the analyses of *Sellers* [1985, 1987] and *Hall et al.* [1990] in the context of the physiological model results summarized in (1) and proposed under normal field conditions the following: First, the mean SR for an area should be near-linearly related to the mean value of FPAR and hence to Π for the same area. This relationship should hold over a wide range of possible nonhomogeneous vegetation distributions within the averaging domain (or sensor field of view), see (6), (7), and (8). Second, for nonsaturating values of the incident PAR flux (F_0), A_c and g_c should be near-linear functions of F_0, see (1).

The arguments of scale independence invoked in (1) and (2) above result from the linearity of the functions linking A_c and g_c to FPAR and FPAR to a suitable SVI. Mathematically, the area integral of a linear function of a variable is identical to the function value of the spatial mean of the same variable over the integrating domain, or

$$\oint g(y)\, ds \equiv g(\langle y \rangle) \oint ds \tag{9}$$

where $g(y)$ is a linear function of y, $\langle y \rangle$ is spatial mean of y over the integrating domain, and s is area.

Because of (9) and the fact that the relationships we are dealing with are near-linear, the functions relating A_c and g_c to SVI should be largely scale-independent.

Given (1) through (9) and the discussion above, we may now write an expression linking the area integrals of the biophysical rates (A_c and g_c) to the area-averaged value of SVI. Thus starting with

$$A_C \text{ or } g_C = \frac{1}{S} \oint^S (A_c \text{ or } g_c)\, ds, \tag{10a}$$

we can adapt (1) to give

$$A_C \text{ or } g_C \propto F_0[B_i]\langle \mathrm{SVI} \rangle, \tag{10b}$$

for

$$F_0 \le F_0^{\mathrm{sat}},$$

where, S is domain of area integration or area averaging, m^2; $[B_i]$ are environmental forcing or feedback terms; and angle brackets denote area average over domain S.

In (10) the subscripted lower case "c" refers to a local-scale canopy quantity, on the scale of a few centimeters or meters. The subscripted capital "C" refers to the area integral of the same quantity (divided by the area of integration) over a much larger domain, say, tens to hundreds of meters, equivalent to the sensor field of view of (or the mean of several pixels from) the remote sensing instrument providing the estimate of the SVI.

A_C and g_C are biophysical quantities that vary depending on vegetation physiology ($V_{\max_0}$), incident PAR flux (F_0), environmental conditions $[B_i]$ and canopy density and architecture (Π), see (1). We can define "unstressed" equivalents of A_C and g_C, denoted by asterisk below, which specify the maximum values of A_C and g_C for given vegetation properties ($V_{\max_0}$, Π) and radiation income (F_0).

$$A_C = A^*_C[B_1, \cdots, B_4] \tag{11a}$$

$$g_C = g^*_C[B_1, \cdots, B_6] \tag{11b}$$

where A^*_C, g^*_C are unstressed canopy photosynthetic rate, conductance.

Equation (11) can then be inserted into (10) and differentiated to yield

$$\phi_F \equiv \frac{\partial A^*_C}{\partial F_0} \propto \langle \mathrm{SVI} \rangle \tag{12a}$$

$$\nabla_F \equiv \frac{\partial g^*_C}{\partial F_0} \propto \langle \mathrm{SVI} \rangle, \tag{12b}$$

for

$$F_0 \leq F_0^{\mathrm{sat}},$$

and where $\phi \equiv \partial A^*_C/\partial$ and $\nabla \equiv \partial g^*_C/\partial$.

The two quantities on the left-hand side of (12) represent conservative properties of the surface which are dependent on the area-averaged physiology and density of the vegetation cover, that is, on $V_{\max_0}$ and Π. They can be expected to vary on the time scale of changes in the vegetation cover, that is, on the time scale of seasons (phenology) and/or climatic stress (droughts, etc.) rather than days. Most importantly, these quantities should be related to a suitable SVI, subject to the condition in (8), in a near-linear and thus scale-independent fashion. However, inspection of the equation set shows that in order to calculate the instantaneous canopy photosynthetic rate or conductance using the SVI, other information must be available for the same time period, principally, the incident PAR flux, F_0, and some knowledge of the variables determining the environmental forcing or feedback terms, B_i.

Equations (11) and (12) represent useful hypotheses that can be tested using the First International Satellite Land Surface Climatology Project (ISLSCP) Field Experiment (FIFE) data. Figure 1 shows schematically how the area-integrated value of the unstressed canopy conductance, g^*_C, might be expected to behave as a function of PAR and increasing canopy greenness.

If the hypotheses represented by (11) and (12) were valid, the response of the area-averaged unstressed surface conductance, g^*_C, to varying PAR loads would depend linearly on the amount of green vegetation present (FPAR or Π), as shown in Figure 1a. Essentially, a biologically inert surface (senescent vegetation, concrete, bare soil) would show no response in g^*_C for a change in F_0, while a green surface would not only show higher values of g^*_C generally but would also show a steep increase in the value of g^*_C for an increase in F_0 when $F_0 < F_0^{\mathrm{sat}}$. At any given time, however, $g_C \leq g^*_C$ because of the stress terms referred to above; g^*_C therefore represents the maximum conductance that can be supported by the vegetated surface. From Figure 1a we see that it is the derivative of g^*_C with respect to incident PAR, ∇_F, that is directly related to the amount of live vegetation on the surface. Figure 1b shows these derivatives for the three surface conditions shown in Figure 1a plotted against an area-averaged SVI for the same area. According to the hypothesis of *Sellers et al.* [1992], there should be a near-linear relationship between the two quantities.

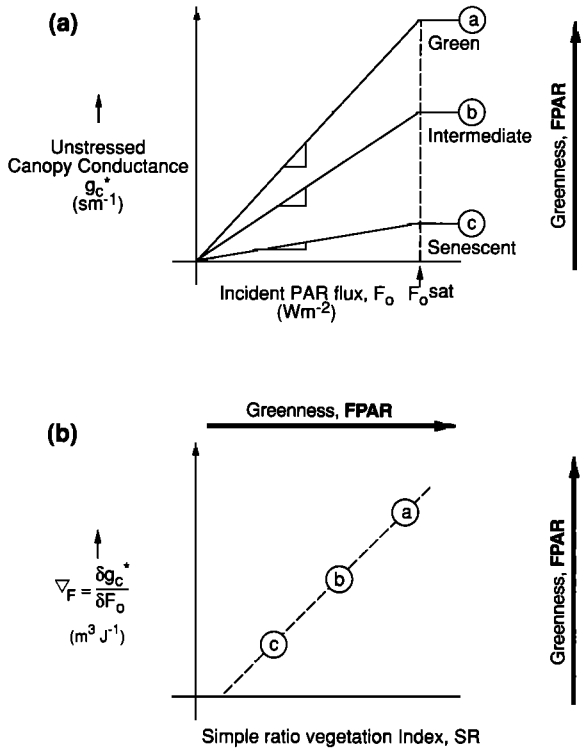

Fig. 1. Schematic figures illustrating the hypothesized relationships between the unstressed canopy conductance, g^*_C, and the simple ratio (SR) vegetation index. (a) Changes in unstressed canopy conductance, g^*_C, for a range of canopy states and incident photosynthetically active radiation (PAR) fluxes, F_0. Note that all the canopy conductances saturate at the same level of F_0, F_0^{sat}, that is, $V_{\max_0}$ is invariant in this example. Derivatives of g^*_C with respect to F_0 ($F_0 < F_0^{\mathrm{sat}}$) are shown. (b) Derivatives of g^*_C with respect to F_0, $\nabla_F \equiv \partial g^*_C/\partial F_0$, plotted against SR vegetation index. The letters on the line correspond to the cases shown in Figure 1a. These figures illustrate the principles shown in (1) to (13), as proposed by *Sellers et al.* [1992]; they contain no real data.

In the study of *Sellers et al.* [1992] the environmental forcing and feedback terms, B_i in (1), were defined on the basis of the analyses of *Farquhar et al.* [1980] and *Collatz et al.* [1991] which take explicit account of the interactions between the leaf interior sites of photosynthesis, leaf stomatal function, and the exterior environment. In the FIFE 87 data set there were only two stations that measured CO_2 flux, so a comprehensive analysis of all the flux site data

using this complete physiological model is impractical. Instead, we can replace the functions B_i by "stress" terms, $f(x_i)$, where $f(x_i)$ are empirical functions which account for the effects of vapor pressure deficit, $f(\delta e)$, temperature, $f(T)$, and soil moisture deficit, $f(\psi)$, separate from any direct consideration of photosynthesis.

We can then write

$$g_C = g_C^* f(x_i) \tag{13a}$$

$$g_C = \nabla_F F_0 f(x_i), \tag{13b}$$

for $F_0 \leq F_0^{\text{sat}}$.

Verma et al. [1992] fitted a function to porometer observations made on the leaves of several species of grass at site 16 (4439-ECV) in FIFE 87 to give an average expression for $f(\delta e)$, the stress term accounting for the effect of vapor pressure deficit.

$$f(\delta e) = \frac{1}{1 + b\delta e}, \tag{14a}$$

where δe is vapor pressure deficit in the canopy air space, Pa, and b is 0.0002 Pa^{-1}.

Observations reported by *Verma et al.* [1992] also include an analysis of the response of the grass to soil water potential. This has been used to formulate a simple expression for $f(\psi)$.

$$f(\psi) = \frac{\psi_m - \psi_{c_2}}{\psi_{c_1} - \psi_{c_2}} \tag{14b}$$

where ψ_m is maximum soil moisture potential in the soil profile, m, and ψ_{c_1}, ψ_{c_2} are leaf water potentials at which stomates start to close and are completely closed, respectively, m.

From the results reported in the work of *Verma et al.* [1992], it is clear that we do not understand exactly how plants respond to acute soil moisture stress. Fortunately, $f(\psi)$ plays only a minor role in the analysis presented in this paper. *Verma et al.* [1992] did not propose an expression for $f(T)$ on the basis of the FIFE data, and *Polley et al.* [this issue] also report that the dependence of leaf photosynthesis on temperature was weak for the C_4 species in the FIFE area. In this study, $f(T)$ was set to unity.

Figure 2 shows a diurnal cycle of heat fluxes and conductances observed and calculated for site 18 (4439-BRV). Here, the total conductance for the site was calculated from the observed meteorological forcings (air temperature, vapor pressure, wind speed) and the observed fluxes by inverting the flux equations

$$H = \frac{(T_s - T_r)}{r_a} \rho C_p \tag{15a}$$

$$\lambda E = \left(\frac{e^*(T_s) - e_r}{r_a + r_T} \right) \frac{\rho C_p}{\gamma} \tag{15b}$$

where

H = sensible heat flux, W m^{-2};
T_s = surface temperature, K;
T_r = air temperature at measurement height, K;
r_a = aerodynamic resistance, s m^{-1};
ρ, C_p = density, specific heat of air, respectively, kg m^{-3} J kg^{-1} K^{-1};
E = evapotranspiration rate, kg m^{-2} s^{-1};
λ = latent heat of vaporization, J kg^{-1};
γ = psychrometric constant, Pa;
$e^*(T_s)$ = saturation vapor pressure at surface temperature, T_s, Pa;
e_r = vapor pressure at reference height, Pa;
r_T = total surface resistance, s m^{-1};
$r_T = 1/g_C$ when soil evaporation is zero.

For the case shown in Figure 2, H and T_r are supplied by measurements from site 18, r_a is estimated from H, u_r, and an estimate of z_0, following the methods described in the works of *Sellers et al.* [1986, 1989]; and so T_s can be derived from the inversion of (15*a*). (Note that this is an aerodynamic surface temperature rather than a radiometric one; see papers in the Surface Radiances and Biology section of this issue and *Hall et al.* [this issue].) This value of T_s is inserted into (15*b*) along with the measurements of λE and e_r to solve for the total surface resistance term, r_T, which is made up of soil and vegetation components. For illustration the inverse of this derived total resistance ($r_T \simeq 1/g_C$ when soil evaporation is zero) is plotted against PAR in Figure 2*d*. If we assume that the soil evaporation rate is negligible, (13) and (14) can be combined to estimate the equivalent values of g_C^*. It can be seen from Figures 2*c* and 2*d* that g_C^* is more or less linear with incident PAR, but the intercept is nonzero, indicating that there was still a significant soil evaporation contribution three days after the last rainfall (day 154). *Verma et al.* [1992] report similar results. Clearly, a more rigorous analytical technique must be applied to the flux station data to extract g_C^* estimates which are related solely to the transpiration component of the total latent heat flux. These "vegetation-only" values of g_C^* can then be directly compared with remotely sensed SVI to test the hypotheses summarized here in (12) and discussed in full by *Sellers et al.* [1992].

3. Analysis of the Flux Station Data

The FIFE 87 flux station data were analyzed by using a soil-plant-atmosphere model (SiB) in the inverse mode to obtain estimates of ∇_F (abbreviation for $\partial g_C^*/\partial F_0$) for each station for at least 1 day per intensive field campaign (IFC). As part of the analysis the following tasks were performed:

1. The simple biosphere (SiB) model of *Sellers et al.* [1986] was modified to operate in the inverse mode; that is, it was embedded within an optimization procedure so that for any given site and day, values of ∇_F could be derived that would produce the best match between observed and calculated latent heat fluxes (see section 3.1).
2. The original flux station data, the meteorological forcings, and the radiation flux measurements to be used in the analysis were passed through a filtering procedure to screen out data segments containing obvious errors, large data gaps, or precipitation events (see section 3.2).
3. The SiB soil evaporation model was modified and calibrated against the FIFE 87 observations. This model was then inserted into the inverse mode version of SiB (see section 3.3).
4. The modified SiB model was used to calculate ∇_F values for each flux station for at least 1 day per IFC. Incorporation of the soil model described in section 3.3

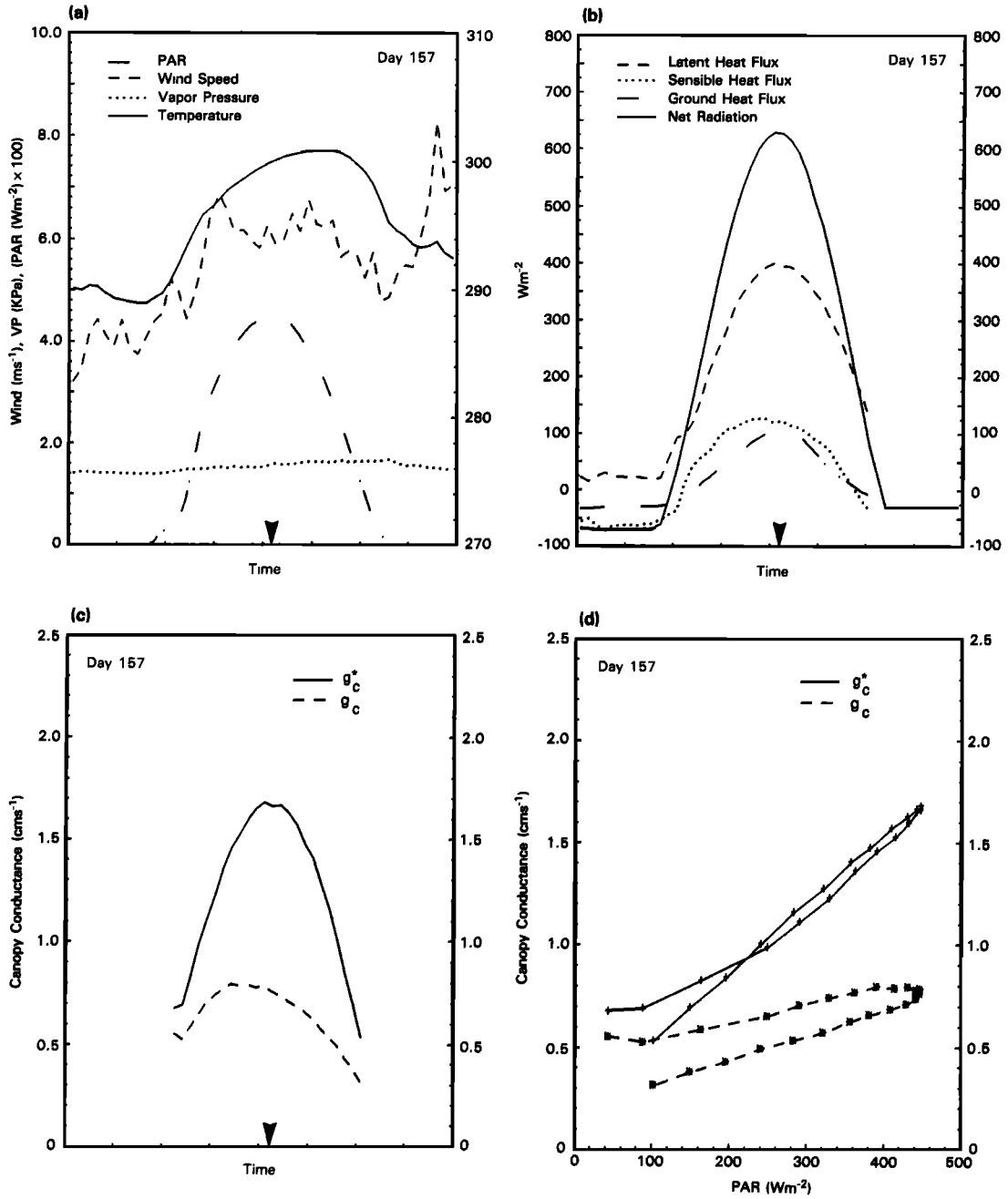

Fig. 2. Diurnal cycle of observed meteorological conditions and energy fluxes at site 18 (4439-BRV) for June 6, 1987, day 157. (From *Verma et al.* [1992]; SF-6.) (*a*) Meteorological forcings: incident PAR, F_0; wind speed, u_r; air temperature, T_r; and vapor pressure, e_r. (*b*) Energy fluxes: net radiation, R_n; latent heat flux, λE; sensible heat flux, H; and ground heat flux, G. (*c*) Conductances: actual and unstressed values of canopy conductance, g^*_C. Note that the soil evaporation was assumed to be zero for the derivation of g_C, g^*_C in this figure. (*d*) Conductances versus incident PAR, replotted from (*a*) and (*c*). Compare the trajectory of g^*_C to Figure 1*a*. The downward solid arrow denotes solar noon.

permitted the estimation of g^*_C values which relate only to the transpiration flux and thus led to the calculation of vegetation-only ∇_F values (see section 3.4).

5. The derived ∇_F values were reviewed. The uncertainties in ∇_F, due to uncertainties in the soil moisture model and the inversion method itself, and random errors in the flux data, were estimated. Estimates of ∇_F associated with large uncertainties were dropped from further analysis (see section 3.5).

These tasks are described in detail in the sections below. The resulting ∇_F values are then compared to the spectral data in section 4.

3.1. *Calculation of ∇_F Values Using SiB in the Inverse Mode*

The simple biosphere (SiB) model of *Sellers et al.* [1986] is a soil-plant-atmosphere model which was originally designed for use within atmospheric general circulation models (GCMs); it is also suitable for some micrometeorological

studies, see Figure 3. The original GCM version of the model consists of two vegetation layers and three soil layers and holds prognostic values of canopy temperature, T_c; ground temperature, T_{gs}; deep soil temperature, Td; three soil wetness values, W_1, W_2, and W_3; and two interception moisture stores, M_c and M_g (M_c and M_g are not relevant to this study).

SiB can be run separately from a GCM if the upper boundary conditions of temperature, T_r, vapor pressure, e_r, wind speed, u_r, downwelling radiation, $R_{\lambda,\mu}$, and precipitation, P, are specified. In this case, the model prognostic variables are initialized from observations: T_c and T_{gs} are set to T_r; T_d to a soil temperature measurement; W_1, W_2, and W_3 to field measurements (gravimetric samples or neutron probe observations); M_c and M_g to zero. The model is then forced with the time series T_r, e_r, u_r, $R_{\lambda,\mu}$, and P and will calculate fluxes of net radiation, R_n, sensible heat flux, H, latent heat flux, λE, and ground heat flux, G. In the process the model calculates a large number of diagnostic variables, such as the canopy air space temperature, T_a, and vapor pressure, e_a, and all of the resistances (inverse of conductances) shown in Figure 3. Most importantly, the soil surface resistance, r_{surf}, is calculated as a function of W_1, and the canopy resistance ($r_c = 1/g_C$) is calculated as a function of vegetation parameters and the forcing variables. At the end of each forcing time step, the prognostic variables are incremented in accordance with energy and moisture conservation principles after which the model is ready to move on to the next time step.

Figure 3 shows how SiB is used in the current application, without a lower story vegetation cover. Note that the model calculates the soil evaporation and canopy transpiration fluxes as separate but interacting quantities connected via

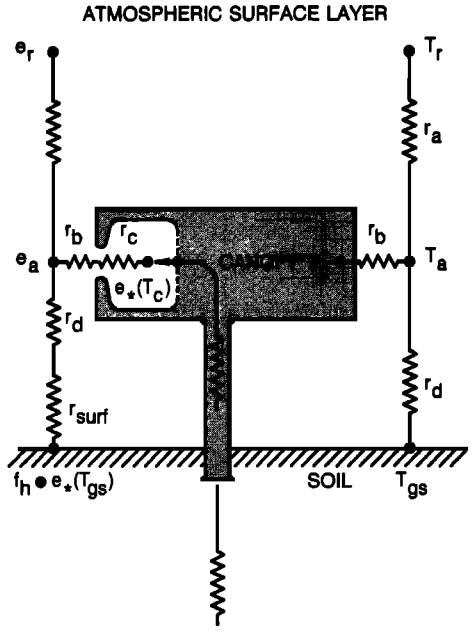

Fig. 3. Schematic diagram of the simple biosphere model (SiB) of *Sellers et al.* [1986] as modified for inverse-mode operation in this study; the ground vegetation cover has been removed and the FIFE site grass canopy has been "promoted" to the upper story. The fluxes of sensible and latent heat flux from the surface to the atmosphere are depicted on the right-hand and left-hand sides of the figure, respectively.

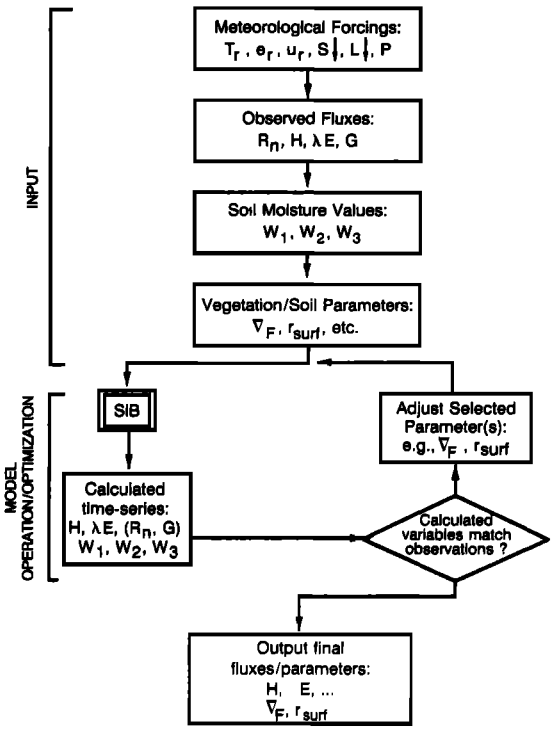

Fig. 4. Operation of SiB in the inverse mode, after *Sellers et al.* [1989].

the aerodynamic resistance network. These fluxes then combine to give an estimate of the total (above-canopy) surface flux which can be compared directly with a flux station measurement. Separate measurement of soil and canopy fluxes is very difficult and was not carried out in FIFE, hence the need for a modeling approach to estimate the canopy contribution to the total flux.

Some modifications were made to the original SiB formulation as described by *Sellers et al.* [1986, 1989] for this application.

1. The second (lower) story of vegetation was omitted. The grass canopy cover was represented by the upper story (subscript "c"); soil fluxes were represented by the ground contribution (subscript "gs").

2. The light-dependent portion of the canopy conductance calculation was replaced by

$$g_C^* = \nabla_F F_0, \tag{16}$$

in accordance with (13b) and the analysis of *Sellers et al.* [1992], where F_0 is the downward PAR flux, as measured by the super automatic meteorological station (AMS); g_C^* is multiplied by the stress terms of (14) to yield an estimate of g_C, the actual canopy conductance.

3. The soil evaporation model was modified to provide a closer match to observed time series of fluxes and soil moisture contents.

The procedure outlined at the beginning of this section describes the normal operation of SiB in its "zero-dimensional" form, that is, separate from a GCM. In this mode all the vegetation parameters are specified a priori, and the model then calculates time series of fluxes. In this study, however, the model is operated in the inverse mode. One or a few parameters are selected for optimization and are initialized to arbitrary values. The model is then run and the

TABLE 1*a*. SiB Parameter Values Used for the Study

Vegetation Aerodynamic Property	Value
Canopy height z_2	0.300, m
Roughness length z_0	0.045, m
Zero plane displacement d	0.083, m
Bulk canopy boundary layer resistance parameter C_1	21.340, s m^{-1}
Ground to canopy air space resistance parameter C_2	27.650, s m^{-1}

Leaf area index values and greenness fractions (used for radiative transfer calculations only) were calculated from staff science data and simple ratio (SR) values, see text in section 3.2 and Appendix. See *Sellers et al.* [1986] for full explanation of parameters.

resulting time series of fluxes are compared to observed fluxes. A nonlinear, least squares optimization package is used iteratively to adjust the selected parameters and the model is run repeatedly until the best match between observed and calculated quantities is obtained, at which point the selected parameters are considered to be optimal. This procedure is shown in schematic form in Figure 4 and more details may be found in the work of *Sellers et al.* [1989], which describes the use of SiB in the inverse mode to calculate physiological parameters for a tropical forest site near Manaus, Brazil, using forcing and flux data obtained by *Shuttleworth et al.* [1984*a*, *b*].

3.2. *Preparation of the Flux Station, Meteorological and Surface Parameter Data Sets*

In this application, SiB is forced with meteorological and radiation data collected a few meters above the surface. The model prognostic variables are initialized from field measurements or interpolations, and most of the vegetation and soil parameters are based on observations. Lastly, the observed fluxes are compared with the fluxes calculated by SiB. The sources of the data sets used in the study are briefly described below:

1. *Meteorological and radiation forcing.* T_r, e_r, and u_r, were taken from the flux station records with gaps filled in from the nearest AMS when necessary. Downward shortwave, $S\downarrow$, and longwave, $L\downarrow$, fluxes were taken from the flux station records and the two operational super-AMS sensors, respectively.

2. *Initialization of prognostic variables.* T_c and T_{gs} were set to the first observation of T_r; T_d was set to the observed 20-cm soil temperature value. M_c and M_g were set to zero. Surface gravimetric values (upper 5 cm) were used to initialize W_1 and neutron probe measurements were used to initialize W_2 and W_3.

3. *Vegetation parameters.* The SiB preprocessor (see *Sellers et al.* [1989] for details) was run using an average vegetation morphological data set obtained from the FIFE Information System (FIS) to calculate the aerodynamic parameters required for the model, see Table 1*a*. Leaf optical properties were obtained from E. A. Walter-Shea (personal communication, 1992; SRB-2). In situ measurements and Landsat SR data were used to estimate canopy leaf area index, canopy greenness, and litter leaf area index values for canopy radiation (albedo, transmittance) calculations, see Table 1b and appendix for details.

4. *Soil physical properties.* The soil physical properties of porosity, θ_s, saturation moisture potential, ψ_s, sorption parameter, B, saturated hydraulic conductivity, K_s, and visible and near-infrared soil surface reflectances were assigned default values on the basis of the FIFE staff science soil survey work and the figures of *Clapp and Hornberger* [1978], see Table 1*c*.

5. *Fluxes.* The fluxes of R_n, H, λE, and, where available, G were taken from each flux station data record as held in FIS (The July 1990 FIS baseline surface flux data set was

TABLE 1*b*. Leaf Area Indexes, Greenness Fractions, Green Leaf Area Indexes, and Litter Layer Leaf Area Indexes

		Canopy Leaf Area Index				Canopy Greenness				Canopy Green Leaf Area Index				Litter Layer Leaf Area Index			
Site	Site ID	IFC-1	IFC-2	IFC-3	IFC-4	IFC-1	IFC-2	IFC-3	IFC-4	IFC-1	IFC-2	IFC-3	IFC-4	IFC-1	IFC-2	IFC-3	IFC-4
2	1916-BRS	3.78	4.11	4.87	2.76	0.34	0.30	0.21	0.25	1.29	1.23	1.03	0.69	0.43	0.16	0.17	0.36
10	3414-BRK	...	3.58	3.20	2.02	...	0.86	0.57	0.33	...	3.07	1.82	0.66	...	0.04	0.04	0.10
12	2915-BRK	2.69	3.79	2.93	0.63	0.44	0.42	0.31	0.10	1.18	1.60	0.90	0.06	0.10	0.39	0.82	0.69
14	2516-BRK	2.37	3.31	5.22	1.97	0.42	0.38	0.23	0.19	1.00	1.25	1.21	0.38	0.15	0.25	0.32	0.57
16	4439-ECV	2.14	3.56	2.61	1.43	0.91	0.86	0.65	0.44	1.96	3.07	1.70	0.63	0.16	0.12	0.04	0.05
18	4439-BRV	2.14	3.56	2.61	1.43	0.91	0.86	0.65	0.44	1.96	3.07	1.70	0.63	0.16	0.12	0.04	0.05
20	6340-BRL	2.38	3.76	2.05	2.63	0.87	0.91	0.75	0.26	2.08	3.41	1.54	0.68	0.01	0.01	0.01	0.18
22	4609-ECW	2.32	2.62	2.59	3.27	0.62	0.66	0.46	0.19	1.43	1.72	1.20	0.63	0.17	0.10	0.29	0.23
24	6912-BRW	2.57	3.31	2.85	1.76	0.80	0.80	0.61	0.38	2.05	2.64	1.73	0.67	0.08	0.03	0.46	0.15
26	8739-ECB	2.45	2.35	1.56	1.22	0.66	0.58	0.65	0.47	1.62	1.36	1.01	0.57	0.05	0.29	0.05	0.10
28	6943-ECW	2.24	4.48	2.65	3.32	0.65	0.60	0.52	0.19	1.46	2.67	1.39	0.65	0.19	0.30	0.12	0.26
32	4268-BRK	...	2.09	1.91	1.06	...	0.67	0.54	0.78	...	1.39	1.02	0.83	...	0.07	0.51	0.08
34	3479-BRL	2.44	3.10	2.45	2.61	0.91	0.88	0.54	0.27	2.23	2.74	1.32	0.70	0.01	0.01	0.03	0.34
36	2655-BRL	1.57	2.10	1.54	1.32	0.82	0.80	0.58	0.50	1.29	1.69	0.90	0.65	0.01	0.20	0.10	0.31
38	1478-BRS	1.76	2.74	2.12	1.65	0.84	0.84	0.69	0.43	1.48	2.30	1.47	0.70	0.03	0.12	0.06	0.10
40	1246-BRL	1.74	2.91	1.94	1.66	0.97	0.76	0.64	0.40	1.69	2.22	1.24	0.67	0.02	0.14	0.02	0.25
42	1445-BRL	1.95	3.84	2.42	1.84	0.93	0.79	0.69	0.34	1.82	3.04	1.67	0.62	0.01	0.08	0.02	0.05
44	2043-BRL	2.09	4.04	2.63	1.34	0.77	0.67	0.52	0.50	1.61	2.72	1.38	0.67	0.11	0.15	0.04	0.13

IFC, intensive field campaign.

TABLE 1c. Soil Properties

Property	Value
Soil reflectance	
visible	0.100
near-IR	0.200
Moisture potential at saturation	
Ψ_s	−0.500, m
Sorption parameter	
B	8.000
Saturated hydraulic conductivity	
K_s	1.660×10^{-6}, m s^{-1}
Porosity	
Θ_s	0.430

used. This data set had all the flux station net radiation values adjusted to a mean standard).

All the flux station data collected during the FIFE 87 IFCs were passed through a series of data quality checks with the aim of producing almost continuous records of reliable data for each station for at least 1 day per IFC. This data filtering procedure consisted of the following steps: (1) Exclusion of data taken within 24 hours following precipitation. (2) Exclusion of noisy data: The Bowen ratio flux data often contained large "spikes" near dawn or dusk when the temperature and humidity gradients were small; these data points were deleted by inspection. (3) Exclusion of data with large gaps: Following steps (1) and (2) above, the data time series was checked for continuity. Time series of data with less than 50% quality-assured values during the daylight hours were dropped from further analysis. The surviving flux station data sets are listed in Table 2a.

3.3. *Calibration of the Soil-Water Transport and Evaporation Models*

The three-layer soil model of SiB was modified for the study. The top layer now consists of a surface layer (0–5 cm), a root zone (a few centimeters thick), and an underlying recharge zone (several centimeters thick). Transport between layers is governed by unsaturated flow equations.

$$Q = K\left[\frac{d\psi}{dz} + 1\right], \tag{17a}$$

$$K = K_s W^{2B+3}, \tag{17b}$$

$$\psi = \psi_s W^{-B}, \tag{17c}$$

where

W = soil wetness fraction;
Q = vertical flow, m s^{-1};
K = hydraulic conductivity, m s^{-1};
K_s = value of K at saturation, m s^{-1};
ψ = soil moisture potential, m;
ψ_s = value of ψ at saturation, m;
B = constant dependent on soil texture.

The default soil physical properties were obtained from the FIFE staff science soil survey work and the published values of *Clapp and Hornberger* [1978], see previous section and Table 1c. However, it is well known that soil physical properties can vary by a few orders of magnitude over relatively short distances. When the soil evaporation rate is large, the value of the saturated hydraulic conductivity parameter, K_s, can exert a major influence on the recharge of the surface layer with moisture from lower layers, see (17).

The evaporation of soil water from the topmost layer was originally based on the formulation of *Shu Fen Sun* [1982] and, subsequently, replaced by the model of *Camillo and Gurney* [1986]. This took the form of

$$\lambda E_{\text{soil}} = \left[\frac{he^*(T_{gs}) - e_a}{r_{\text{surf}} + r_d}\right]\frac{\rho C_p}{\gamma} \tag{18a}$$

$$r_{\text{surf}} = f(W_1), \tag{18b}$$

where

λE_{soil} = soil evaporation rate, W m^{-2};
$e^*(T_{gs})$ = saturated vapor pressure at soil temperature, Pa;
h = relative humidity in soil pore space;
e_a = vapor pressure in the canopy air space, Pa;
r_{surf} = soil surface resistance, s m^{-1};

TABLE 2a. Inventory of Flux Station Data Used in This Paper

Location		Day of Year				Location		Day of Year	
Site	Site ID	IFC 1	IFC 2	IFC 3	IFC 4	Site	Site ID	FIFE 89	FIFE 89
2	1916-BRS	155–157	192	229	281	902	1916-BRK	209	216
10	3414-BRK	···	178	229	281	904	2133-BRL	209	216
12	2915-BRK	157	178	229	279	906	2133-ECA	209	216
14	2516-BRK	157	178	229	279	908	2330-BRK	209	216
16	4439-ECV	155–156	178	229	281	910	3317-BRK	209	216
18	4439-BRV	155–157	178	229	279	912	3129-BRK	209	216
20	6340-BRL	155–157	178	229	281	913	6735-BRL	209	216
22	4609-ECW	157	192	229	281	916	4439-ECV	209	216
24	6912-BRW	157	178	229	279	924	6912-BRL	209	216
26	8739-ECB	157–158	178	229	278	926	8739-ECB	209	216
28	6943-ECW	157	178	229	279	932	4268-BRL	209	···
32	4268-BRK	···	178	229	280	936	2655-BRL	209	216
34	3479-BRL	155–157	178	229	279	944	1942-BRL	209	216
36	2655-BRL	155–157	178	229	281				
38	1478-BRS	155–157	192	229	279				
40	1246-BRL	155–157	178	229	278				
42	1445-BRL	155	178	229	280				
44	2043-BRL	155–157	192	229	279				

TABLE 2b. Inventory and Values of Landsat Thematic Mapper (TM) Data

Site	IFC 1, Day 163 SR	IFC 1, Day 163 σ_{SR}	IFC 2, Day 195 SR	IFC 2, Day 195 σ_{SR}	IFC 3, Day 227 SR	IFC 3, Day 227 σ_{SR}	IFC 4, Day 291 SR	IFC 4, Day 291 σ_{SR}	Site	FIFE 89, Day 216 SR	FIFE 89, Day 216 σ_{SR}
2	2.10	0.00	2.02	0.00	1.74	0.00	1.27	0.00	902	1.22	0.04
10	3.85	0.25	4.58	0.51	2.84	0.19	1.23	0.07	904	1.88	0.16
12	3.37	0.74	4.44	1.45	2.86	0.45	1.29	0.06	906	2.06	0.34
14	2.73	0.26	3.59	0.41	2.26	0.15	1.23	0.05	908	2.14	0.21
16	3.03	0.26	4.57	0.39	2.68	0.24	1.19	0.03	910	1.63	0.08
18	3.03	0.26	4.57	0.39	2.68	0.24	1.19	0.03	912	1.72	0.07
20	3.20	0.45	5.05	1.01	2.45	0.35	1.25	0.05	913	2.01	0.13
22	2.29	0.40	2.71	0.51	1.98	0.11	1.18	0.05	916	2.57	0.06
24	3.16	0.20	3.97	0.23	2.72	0.20	1.24	0.05	924	1.70	0.07
26	2.56	...	2.20	...	1.71	...	1.10	...	926	1.89	0.08
28	2.33	0.58	4.02	0.68	2.24	0.39	1.21	0.14	932	2.05	0.17
32	1.88	0.15	2.25	0.18	1.73	0.10	1.46	0.11	936	1.69	0.06
34	3.40	0.27	4.12	0.62	2.14	0.18	1.28	0.07	944	1.57	0.09
36	2.11	0.12	2.66	0.27	1.56	0.06	1.22	0.06			
38	2.37	0.07	3.50	0.31	2.35	0.17	1.29	0.05			
40	2.66	0.28	3.39	0.56	2.04	0.25	1.24	0.05			
42	2.84	0.39	4.54	0.31	2.64	0.11	1.17	0.04			
44	2.54	0.24	4.09	0.61	2.22	0.25	1.24	0.04			

SR refers to the calculated (3 × 3 pixel) mean of the simple ratio vegetation index assigned to each site for the IFC; σ_{SR} refers to the standard deviation of SR associated with that value. Note that sites 2 and 26 σ_{SR} values are missing; the SR values were not extracted from the standard FIFE Information System (FIS) image but provided separately by FIS.

r_d = aerodynamic resistance between soil surface and the canopy air space, s m^{-1};

W_1 = soil wetness of surface layer in original SiB formulation, that is, (0–2 cm).

There are two problems with using these original formulations for K and r_{surf} in the current inverse mode work. First, they were developed using a data set collected over an agricultural bare soil site that had very different soil physical properties from the unplowed Konza Prairie and surrounding pasture areas. Second, the parameterizations were functionally based on the wetness of a thin (0–2 cm or less) upper soil layer, consistent with the original SiB model as used in GCMs; however, the near-surface soil moisture data collected in FIFE 87 consisted of gravimetric (0–5 cm) samples. It was decided therefore to develop a site-specific soil resistance parameterization based on the FIFE 87 data set.

TABLE 2c. Fraction of C_3 Grass Species, V_3 (by Cover Fraction), Reported for Each Site/IFC

Site	IFC 1	IFC 2	IFC 3	IFC 4
2	0.77	0.70	0.52	0.70
10	...	0.40	0.38	0.47
12	0.72	0.69	0.35	0.34
14	0.69	0.49	0.38	0.35
16	0.40	0.38	0.23	0.25
18	0.40	0.38	0.23	0.25
20	0.60	0.36	0.14	0.13
22	0.49	0.42	0.35	0.28
24	0.73	0.60	0.43	0.46
26	0.67	0.62	0.50	0.51
36	0.60	0.57	0.47	0.39
38	0.29	0.41	0.34	0.47

V_3 is given by $C_3/(C_3 + C_4)$, where C_3 and C_4 are the cover fractions of C_3 and C_4 grass species, respectively. The originally anomalous site 22/IFC 3 value has been replaced by the mean of the IFC 2 and IFC 4 values.

Some of the flux stations reported almost continuous time series of forcing variables and flux measurements over a few days in IFCs 1 and 3. These time series were used in the inverse-mode version of SiB to derive values of ∇_F, assumed to be constant over each period of a few days, and r_{surf}, assumed to be constant on any one day. For these runs and other runs described in section 3, the calculated values of R_n and G were forced to match observations. Note that in this procedure, no assumptions need be made about the relationship between r_{surf} and W_1.

Figure 5 shows the results of this work. As expected from other studies, *Shu Fen Sun* [1982], *Camillo and Gurney* [1986], and *Villalobos and Fereres* [1990], r_{surf} increases as W_1 decreases, presumably because the diffusion path length for escaping soil water vapor increases as the soil surface dries out.

The best fit to the points shown in Figure 5 is given by

$$r_{surf} = \exp\,(8.206 - 4.255\ W_1), \qquad (19)$$

where W_1 is wetness of the (0- to 5-cm) layer.

Equation (19) is shown as a solid line in Figure 5, with plus and minus one standard deviations shown as dashed lines.

A subsequent inverse mode run was performed using the site 18, days 155–157 data to derive a representative value of the saturated hydraulic conductivity parameter, K_s. In this run, r_{surf} was described by (19) and optimal values of ∇_F and K_s were determined based on a best fit to observed fluxes (see section 3.4) and observed W_1 values. The final simulations from this run are shown in Figure 6: they indicate that the soil water transport and surface resistance models can provide an adequate description of the soil evaporation contribution. The derived value of K_s is shown in Table 1c. In this simulation the soil evaporation is calculated to make up about a quarter of the first day's total evapotranspiration with a declining contribution thereafter as the upper soil

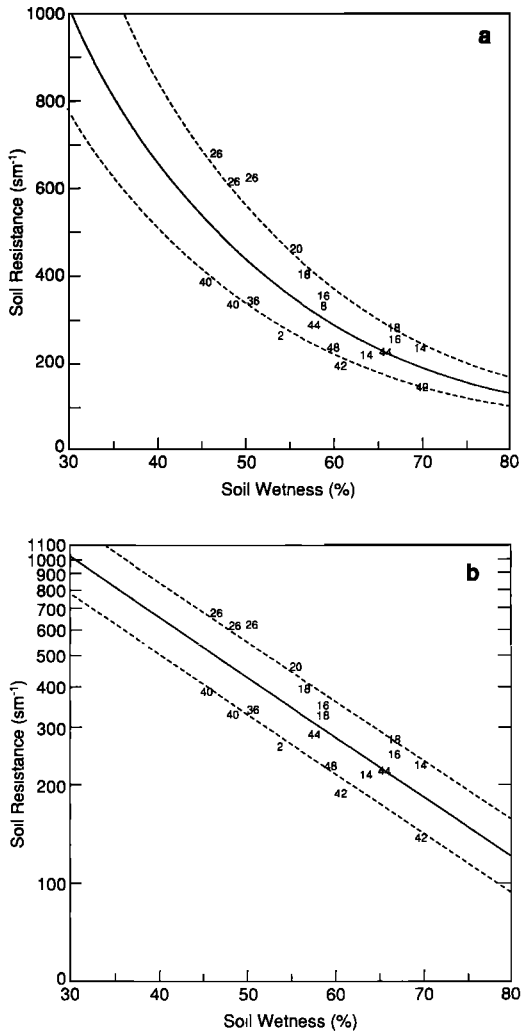

Fig. 5. Soil surface resistance values, r_{surf}, plotted against wetness of the upper soil layer, W_1 (0–5 cm). The r_{surf} values were derived as best fit daily mean values from a series of SiB inverse-mode runs. The W_1 values are taken from the mean of the available (0–5 cm) gravimetric samples for each site for each day; typically, four or five samples were taken. The solid line is the least squares fit to the data; the dotted lines represent one standard deviation on either side of this; see (19) in text. Numbers denote flux station sites; see Table 2. (*a*) Values of r_{surf} plotted against W_1. (*b*) Natural logarithm of r_{surf} plotted against W_1.

layer dries out. This is in approximate agreement with the results of *Villalobos and Fereres* [1990].

For the optimization/simulation tasks described in this section and later, the calculated net radiation and soil heat fluxes were forced to agree with observations, see Figure 6*a*, using techniques described by *Sellers et al.* [1989]. This procedure facilitates the optimization procedure and reduces the effects of possible errors in the canopy and soil radiative transfer calculations due to uncertainties in the surface input parameters (leaf area index, leaf scattering properties, soil reflectance, etc.) listed in Table 1.

3.4. *Calculation of ∇_F for all Flux Stations*

The soil moisture model, as specified in (19), was used throughout in the optimization tasks discussed below.

The standard procedure for each flux station was to choose one or more days of data from each IFC, see Table 2, and obtain optimal values of ∇_F for that station/day by minimizing the difference between the observed and calculated fluxes and evaporative fractions, that is,

$$\text{Minimize} \sum_{i=1}^{M} \left[(\lambda E_0 - \lambda E_p) \left(\frac{1}{|\lambda E_0| + |H_0|} + \frac{1}{50} \right) \right] \qquad (20)$$

$$\lambda E_0 \geq 50$$

where λE_0, λE_p are observed and calculated total latent heat fluxes, W m^{-2}; H_0 is observed total sensible heat flux, W m^{-2}; and M is the number of observed flux points in the flux station time series, where $\lambda E_0 \geq 50$.

In (20) the scaling term represented by "1/50" in the innermost parentheses accounts for the total error between observed and calculated fluxes. The other term in the same parentheses accounts for the error between observed and calculated evaporative fractions and increases the importance of accurate model simulation under low-radiation conditions.

For each run, the observed initial value of W_1 was inserted into (19) to produce a value of r_{surf} for the day of simulation. K_s was set to the value shown in Table 1*c*, and the initialization of prognostic variables was handled in the same way as before. The resulting values of ∇_F are shown in Table 3.

There are two main sources of uncertainty in these estimates of ∇_F. The first is due to uncertainty in the derived soil surface resistance term r_{surf}: Figure 5 shows the uncertainty in r_{surf} for a given value of W_1. The possible error in ∇_F due to uncertainties in r_{surf} was investigated by running the inverse model for three initial surface conditions:

$r_{surf} = f(\langle W_1 \rangle)$. The mean of the available W_1 observations (usually five measurements were made) was used to provide an estimate of r_{surf} using (19).

$r_{surf} = f(\langle W_1 \rangle) + \sigma_r$.

$r_{surf} = f(\langle W_1 \rangle) - \sigma_r$. The run was repeated with initial r_{surf} values set one standard deviation, σ_r, higher and lower than the mean value used in the first run; see Figure 5.

In Figure 9 the ∇_F results corresponding to the $+\sigma_r$ and $-\sigma_r$ runs are shown as solid vertical error bars. The second main source of uncertainty is due to a poor fit of the model to data: If we assume that a correctly calibrated model is capable of providing a perfect description of the surface energy and water balance at a flux station site, then the use of "noisy" flux measurements or meteorological forcing data in the optimization procedure will result in, first, a large residual error, see (20), and second, a slow change in this error away from the minimum, see Figure 7*a*. An index that can be used to describe this uncertainty is the change (positive and negative) in the optimized parameter, in this case ∇_F, necessary to increase the total error value at the minimum by 50%. From Figure 7 we see that this procedure will identify noisy data sets or cases wherever the model provides a poor description of the energy balance. The uncertainty in ∇_F due to this effect is shown in Figure 9 by dashed vertical error bars. This type of error is also reflected in the standard deviation (between observed and simulated) λE and H statistics shown in Table 3.

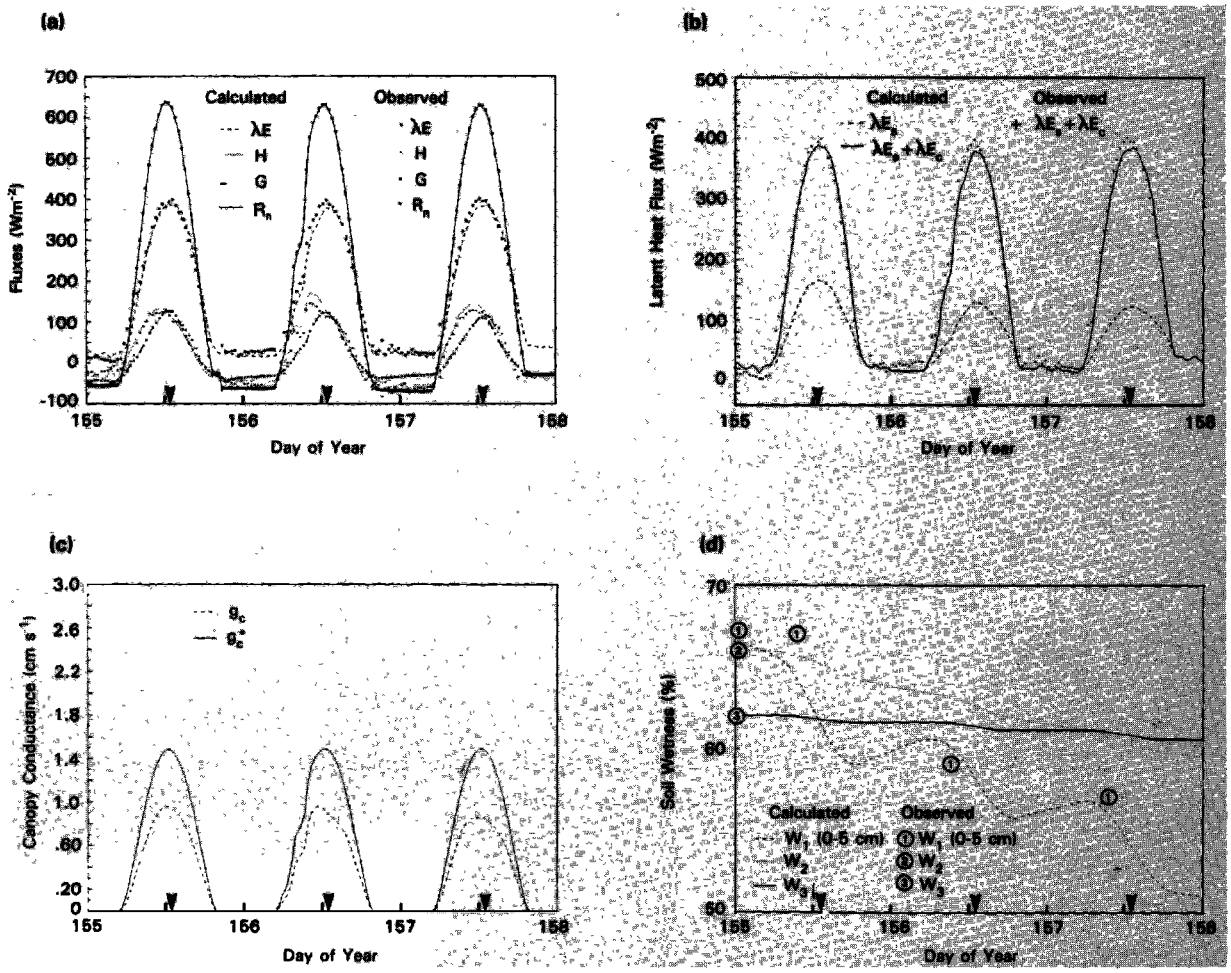

Fig. 6. Comparison of observations and simulations for site 18 (4439-BRV) flux station data, days 155–157. (*a*) Energy fluxes: R_n, H, λE, G. (*b*) Evapotranspiration contributions: soil evaporation, λE_s, and canopy transpiration, λE_0. (*c*) Conductance: canopy conductance, g_c, and unstressed canopy conductance, g_c^*. (*d*) Soil moisture: time series of simulated layer 1 (0–5 cm), layer 2, and layer 3 soil wetness values (W_1, W_2, and W_3). Observed soil wetness values are shown as circles.

Figures 7*b* and 7*c* provide a more graphic illustration of how the two uncertainties appear in the "error space" of the optimization procedure. Note that the contours of the error field are more or less aligned along a valley defined by the shape of the soil surface resistance curve (compare with Figure 5). This means that for a given value of r_{surf} a value of ∇_F can be found (in the valley bottom) that will give an error value close to that of the global minimum. This result makes good sense as soil and plant evaporation rates can compensate for each other to quite a large degree, see *Villalobos and Fereres* [1990]. The figures also show how each of the two errors discussed above appear in the error space; note that the site 26, day 157, error field is broader than that for site 18, due to a poorer fit of the model to the site 26 data for this particular day.

3.5. *Review of Calculated ∇_F Values*

The ∇_F values shown in Table 3 are plotted against time for each individual station in Figure 8*a* and against SR in Figures 9*a* through 9*r* (in Figures 8 and 9 the values of ∇_F have been connected with straight lines to allow the reader to distinguish one set of station results from another; the actual trajectories of ∇_F may be quite different). All the stations show similar trends which may be summarized as follows: (1) A seasonal trend, with maximum ∇_F values in IFCs 1 and 2, decreasing to minimum values in IFC 4, consistent with the vegetation phenology and soil moisture time history, see Figure 8*a*. (2) Large uncertainties in many of the IFC 1 and some of the IFC 2 ∇_F values due to uncertainties in r_{surf} and the inversion procedure (goodness of fit). This indicates that the soil evaporation model may be the source of large uncertainties and/or errors in the derived value of ∇_F under wet soil conditions, see Figure 9. (3) Lower uncertainties in most of the ∇_F values for IFC 3, probably because of the reduced soil evaporation contribution, see Figure 9. (4) Large (relative) uncertainties in ∇_F values for IFC 4, probably because of the sensitivity of the modeled fluxes to small changes in W_1 and r_{surf} under these conditions. Some stations also exhibit unrealistically large values of ∇_F in IFC 4 due to an overestimation of λE, suggestive of a systematic bias in some of the flux data, see Figure 9.

On the basis of the above results some of the derived ∇_F values were dropped from further analysis using the follow-

TABLE 3. Calculated ∇_F and r_{surf} Values for Flux Station Days in FIFE 87

Site	DOY	∇_F	r_{surf}	W_1	$\sigma_{\lambda E}$	σ_H	Deleted
			(a) IFC 1				
2	157	0.258E−04	455.	0.490	10.2	11.3	
10	...	...	...	...	...	...	
12	157	0.178E−04	179.	0.710	19.8	16.3	
14	157	0.746E−05	186.	0.700	7.7	7.0	
16	156	0.357E−04	298.	0.590	25.9	22.1	
18	157	0.295E−04	324.	0.570	15.6	13.7	
20	157	0.745E−04	368.	0.540	31.8	29.8	**
22	157	0.437E−04	353.	0.550	22.8	25.0	
24	157	0.645E−04	588.	0.430	44.4	41.3	**
26	157	0.440E−04	455.	0.490	15.6	11.7	
28	157	0.234E−04	298.	0.590	26.4	28.6	**
32	...	...	...	...	...	...	**
34	157	0.342E−04	384.	0.530	25.7	26.9	**
36	157	0.598E−04	475	0.480	29.4	27.6	**
38	157	0.440E−04	588.	0.430	30.6	28.5	**
40	157	0.322E−04	517.	0.460	16.6	15.9	**
42	155	0.343E−04	273.	0.610	14.2	12.2	**
44	157	0.337E−04	310.	0.580	9.2	8.4	**
			(b) IFC 2				
2	192	0.243E−04	517.	0.460	26.1	26.6	
10	178	0.430E−04	401.	0.520	18.7	15.6	
12	178	0.335E−04	221.	0.660	7.8	7.3	
14	178	0.179E−04	179.	0.710	9.4	11.0	
16	178	0.338E−04	194.	0.690	18.7	15.8	
18	178	0.297E−04	194.	0.690	17.5	13.7	
20	178	0.335E−04	151.	0.750	18.3	15.8	
22	192	0.320E−04	455.	0.490	18.7	15.6	
24	178	0.418E−04	251.	0.630	31.9	27.5	**
26	178	0.472E−04	640.	0.410	20.1	14.3	
28	178	0.166E−04	94.	0.860	16.5	20.2	**
32	178	0.234E−04	368.	0.540	15.5	15.1	**
34	178	0.186E−04	194.	0.690	29.2	31.6	**
36	178	0.480E−04	273.	0.610	22.6	20.3	
38	192	0.342E−04	668.	0.400	18.1	16.0	
40	178	0.302E−04	262.	0.620	12.0	12.1	**
42	178	0.176E−04	151.	0.750	21.3	18.9	**
44	192	0.510E−04	588.	0.430	14.9	13.0	**
			(c) IFC 3				
2	229	0.118E−04	368.	0.540	10.5	13.4	
10	229	0.315E−04	298.	0.590	23.5	21.1	
12	229	0.123E−04	273.	0.610	19.4	23.6	
14	229	0.120E−04	241.	0.640	11.5	13.1	
16	229	0.153E−04	241.	0.640	23.7	19.7	
18	229	0.156E−04	241.	0.640	25.3	21.5	
20	229	0.153E−04	338.	0.560	15.7	13.1	
22	229	0.154E−04	324.	0.570	11.0	10.1	
24	229	0.263E−04	285.	0.600	19.3	15.9	
26	229	0.166E−04	418.	0.510	8.2	5.0	
28	229	0.130E−04	298.	0.590	26.7	29.9	**
32	229	0.274E−04	540.	0.450	24.3	26.6	**
34	229	0.149E−04	262.	0.620	38.1	39.9	**
36	229	0.237E−04	418.	0.510	11.3	10.1	
38	229	0.196E−04	324.	0.570	18.3	19.1	
40	229	0.267E−04	368.	0.540	18.0	20.7	**
42	229	0.107E−04	186.	0.700	9.3	12.6	**
44	229	0.313E−04	353.	0.550	17.4	20.7	**
			(d) IFC 4				
2	281	0.113E−04	1066.	0.290	7.3	9.5	
10	281	0.869E−05	1499.	0.210	5.5	7.1	
12	279	0.298E−05	455.	0.490	12.9	13.7	
14	279	0.730E−05	668.	0.400	8.6	11.2	
16	281	0.616E−05	979.	0.310	4.7	6.6	
18	279	0.759E−05	900.	0.330	8.9	10.7	
20	281	0.945E−05	862.	0.340	12.0	9.3	
22	281	0.444E−05	979.	0.310	4.4	7.4	
24	279	0.429E−05	1161.	0.270	8.2	7.7	
26	278	0.103E−04	1212.	0.260	12.6	11.3	
28	279	0.104E−04	826.	0.350	21.5	24.7	**
32	280	0.137E−04	1854.	0.160	8.2	7.0	**
34	279	0.120E−04	727.	0.380	47.0	51.6	**
36	281	0.850E−05	900.	0.330	8.1	10.4	
38	279	0.331E−05	759.	0.370	10.1	8.5	
40	278	0.145E−04	939.	0.320	18.1	17.3	**
42	280	0.117E−04	668.	0.400	20.3	23.0	**
44	279	0.234E−04	1264.	0.250	11.6	13.2	**

DOY, day of year. Read 0.258E−04 as 0.258×10^{-4}. The r_{surf} values refer to mean soil surface resistance values used in the inverse-mode runs; $r_{surf} = f(W_1)$; see (19). Initial values of W_1 are listed in the table. The standard deviations for latent heat fluxes, $\sigma_{\lambda E}$, and sensible heat fluxes, σ_H, refer to the goodness of fit between observed and simulated fluxes (W m^{-2}). Asterisks in the "deleted" column refer to ∇_F values that were not used in further analyses; see text in section 3.5.

ing criteria. (1) Poor model fit: Table 3 shows the standard deviations (between observed and calculated fluxes) for each of the inverse model runs. The ∇_F values associated with heat flux standard deviations of greater than 27.5 W m^{-2} were excluded from further analyses. (2) Suspected measurement bias: Some stations reported anomalously high latent heat fluxes during IFC 4, indicating a possible problem with their measurement systems. Stations associated with IFC 4 ∇_F values of 1.2×10^{-5} m^3 J^{-1} or greater, or where the heat flux standard deviations were greater than 20 W m^{-2} for ∇_F values greater than or equal to 1.0×10^{-5} m^3 J^{-1}, were excluded from further analysis (sites 28, 32, 34, 40, 42, and 44).

The excluded values are marked with asterisks in the "deleted" column of Table 3. The surviving ∇_F values are shown in Figures 8*b* and 9*t*.

4. Comparison of ∇_F With SVI Values and Vegetation Properties (C_3/C_4 Ratio)

Hall et al. [1991] describe how the FIFE 87 and FIFE 89 Landsat TM data were radiometrically rectified to provide a self-consistent series of radiance images that appear to have been acquired through a single reference atmosphere. For the FIFE 87 analyses discussed here, the Landsat scenes closest to each IFC were taken to be representative of conditions for that IFC, see Table 2*b*. The channel 3 and 4 radiances from the rectified images were used to calculate SVIs (SR and ND) for a 3 × 3 pixel area centered on each flux station site, an area of roughly 90 m × 90 m or broadly representative of the flux site "footprint," as defined by *Schuepp et al.* [1990].

Figure 9 shows the derived ∇_F time series for all the flux stations listed in Table 3 plotted against the SR value appropriate to each IFC. Some obvious trends are apparent: (1) High linear correlation between the SR vegetation index and ∇_F for each station on a station-by-station basis. (2) The data divide into groups on the basis of the slope of ∇_F versus SR. Stations 2, 26, and 36 have relatively high slopes; stations 12, 14, 16, 18, and 20 have low slopes; and stations 10, 22, 24, and 38 are intermediate. These groups are identified by the solid (high slope), dashed (low slope), and dotted (intermediate slope) lines in Figures 9*s* and 9*t*. (3) Stations 16 and 18 (low-slope group) show an increase in SR during the transition from IFC 1 to IFC 2 for little or no change in ∇_F.

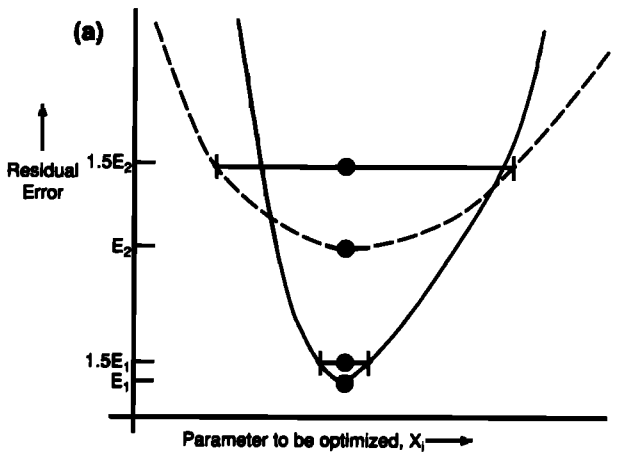

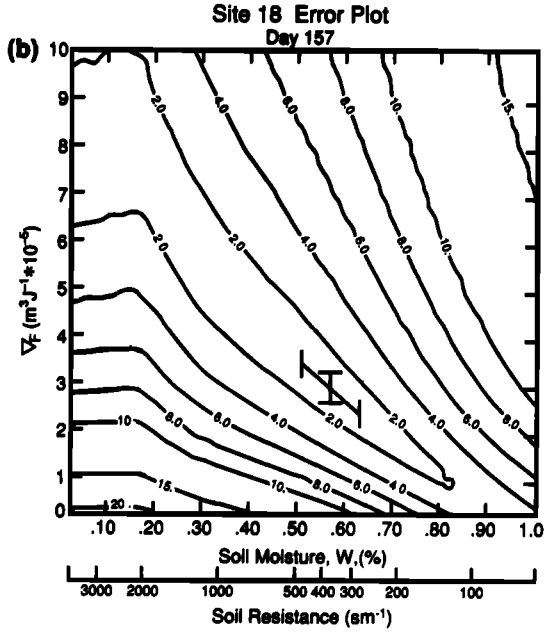

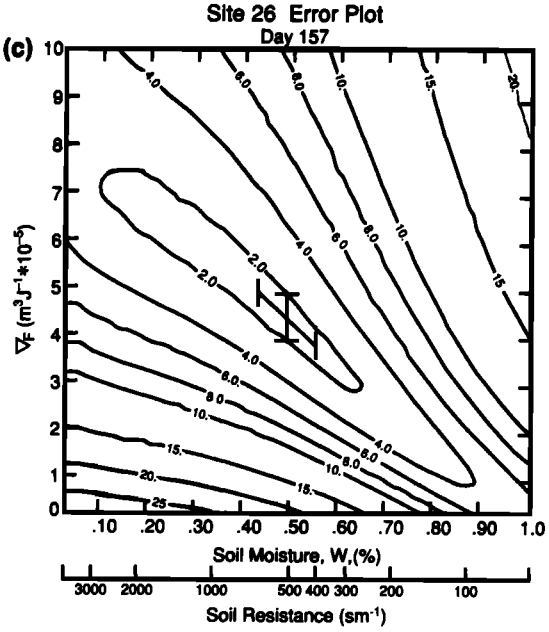

It can be argued that the differences between the ∇_F versus the SR slopes for the stations shown in Figure 9 may be partially due to biases associated with the different flux measurement systems. Some numerical sensitivity analyses indicated that a large bias in the measured evaporation fraction of 10% could result in a bias in the (inverse model) retrieved value of ∇_F of the order of 10^{-5} m^3 J^{-1}, or about 30% of ∇_F (site 18, day 157). However, even extreme errors (biases) of this nature are not sufficient to support the hypothesis that all the points in Figure 9 should line up on the same straight line; that is, the separation between the low-slope and the high-slope groups in Figure 9 is almost certainly real, see also *Stewart and Verma* [this issue]. Further support for this view may be obtained by inspecting the ∇_F versus SR trajectories for sites 18 (4439-BRV) and 16 (4439-ECV): these colocated stations used different flux measurement techniques (Bowen ratio and eddy correlation, respectively) but yielded very similar ∇_F values over the growing season, well within each other's range of uncertainty.

The findings in point 1 above are consistent with the theoretical studies of *Sellers* [1987] and *Sellers et al.* [1992] reviewed in section 1; that is, ∇_F is proportional to SR, see (12). Straight-line fits were made to the IFCs 2, 3, and 4 station values shown in Figure 9, see Table 4. In Tables 4*a* and 4*b* the fits were applied independently to each set of station ∇_F versus SVI data. However, it is reasonable to assume that completely dead vegetation has a ∇_F value of zero and a uniform SVI value over the FIFE area (although burned and unburned treatments might modulate this). Accordingly, in Tables 4*c* and 4*d*, the linear fits to the station values were constrained to pass through a best fit common value of SVI (or pivot point) on the $\nabla_F = 0$ axis. In the rest of this paper the fits shown in Table 4*c* will be scrutinized as they conform to this general "single-pivot" model and because, for this case at least, the use of SR appears to give a more linear relationship with ∇_F than ND; the mean standard deviation of ∇_F versus the SVI was 0.382 for SR in Table 4*c*, as opposed to 0.440 for ND in Table 4*d*. As the SR is near-linearly related to FPAR (see papers in the Surface Radiance and Biology section of this journal and *Sellers* [1987]), the slopes of these lines, referred to as $\nabla_{S,F}$ values from now on, are indices of the change in ∇_F for a change in FPAR. We can write

Fig. 7. (Opposite) Variation of residuals (errors) with independent variables (parameters being optimized). (*a*) Illustration of variation of a typical residual (e.g., (20)) with a variable X_i (e.g., ∇_F) for different data set qualities. (Solid curve) High-quality data and good match of model to data; low minimum value of residual with sharp increase as X_i moves away from minimum. (Short-dashed curve) Noisy data or poor match of model to data; high minimum value of residual with only a gradual change as X_i moves away from minimum. The uncertainties in X_i, as defined in the text for ∇_F, are shown here for both of the above curves as horizontal error bars. They correspond to the spread in X_i (positive and negative) necessary to increase the minimum residual values by 50%. (*b*) Residual field for site 18 (4439-BRV), day 157. Contours represent values of residual (equation (20)) for different input values of r_{surf} and ∇_F; note the well-developed and elongated minimum; r_{surf} and model fit uncertainties are marked as diagonal and vertical error bars, respectively, and crossover on the global minimum, that is, the solution. (*c*) Residual field for site 26 (8739-ECB), day 157. The symbols are the same as in 7*b*. The minimum is less well developed and the uncertainties are slightly larger for this site/day.

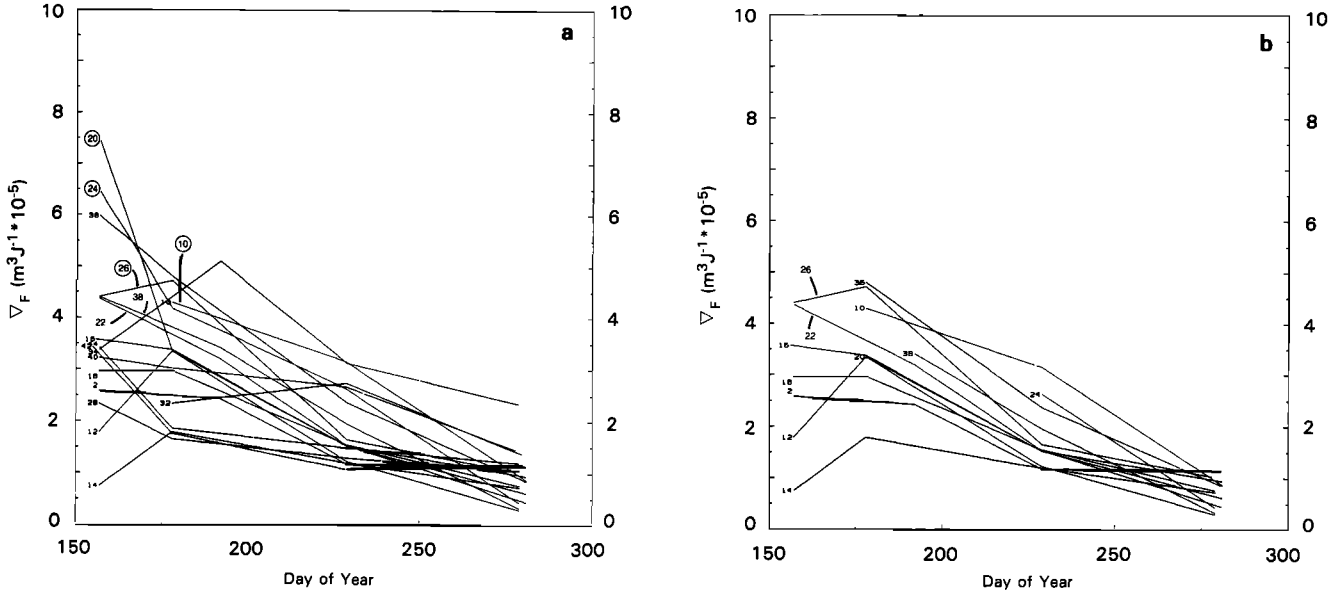

Fig. 8. Derived ∇_F values plotted against time for FIFE 87 flux stations. (*a*) All stations/dates listed in Table 3. (*b*) Selected stations, that is, stations marked with asterisks in Table 3 have been omitted (see section 3.5).

$$\nabla_{S,F} \equiv \frac{\partial \nabla_F}{\partial(\mathrm{SR})} \equiv \frac{\partial}{\partial(\mathrm{SR})}\left(\frac{\partial g_c^*}{\partial F_0}\right) \propto \frac{\partial \nabla_F}{\partial(\mathrm{FPAR})}. \quad (21)$$

Inspection of Figure 9, Table 4, and (21) indicates that while the selected stations have similar values of ∇_F during each FIFE 87 IFC, they are associated with a range of FPAR values, as specified by SR. Put another way, the range of $\nabla_{S,F}$ values suggests that the vegetation around different stations can achieve comparable ∇_F values with very different values of FPAR. This requires some explanation.

Of the "high-slope" group, site 2 is a managed pasture, and sites 26 and 36 were very heavily grazed in 1987 (T. Seastedt, personal communication, 1991). The other stations were all less heavily grazed than sites 26 and 36, which suggests that management practice at and around each site may influence the ∇_F versus SR relationship.

Table 2*c* shows the seasonal progression of the percentage of C_3 species for each selected station, based on species survey data held in FIS. At many sites there is a relatively high cover fraction of C_3 species at the beginning of the growing season which gradually falls off as heat-tolerant C_4 species prosper during the summer. Additionally, sites 2, 26, and 36 have high-C_3 cover fractions throughout the entire year, probably associated with seeding (site 2) and grazing (sites 26 and 36). C_4 species are capable of maintaining a much lower internal CO_2 concentration than C_3 species (roughly 0.4 as compared to 0.7 times atmospheric CO_2 concentration, respectively) which means that for the same area-averaged stomatal conductance and hence transpiration rate, a C_4 cover can draw down much more CO_2 than a C_3 cover. Alternatively, given the same water resources, water rationing strategy, and meteorological conditions, a C_4 cover should support a more extensive canopy or more FPAR than a C_3 cover to give the same value of g_C^*.

This principle can be investigated further using the *Collatz et al.* [1991] leaf conductance-photosynthesis model:

$$g_s = \frac{mA}{C_s} h_s + b, \quad (22)$$

where

g_s = leaf stomatal conductance, mol m^{-2} s^{-1};
m = slope parameter;
$m \simeq 9$ for C_3 species;
$m = 3$ to 4 for C_4 species;
A = leaf assimilation rate, mol m^{-2} m^{-1};
h_s = relative humidity at the leaf surface;
C_s = CO_2 concentation at the leaf surface, mol mol $^{-1}$;
b = constant;
$b \simeq 0.01$, mol m^{-2} s^{-1}.

Equation (22) is the semiempirical core of the *Collatz et al.* [1991] conductance model and has proved to be a robust description of the links among photosynthesis, conductance, and the leaf environment. In canopy-integral form, (22) is implicit in the canopy-scale model of *Sellers et al.* [1992]; see (1). The value of m has been shown from observations to be approximately 9 for C_3 species and between 3 and 4 for C_4 species; see also *Polley et al.* [this issue]. In proceeding from the leaf-scale models to a canopy-scale model, *Sellers et al.* [1992] found that the physiological contributions to A_C and g_C were effectively separable from the canopy morphological (Π) contribution, and so we might expect that for a given value of FPAR, or SVI, a C_3 cover would have roughly 2 or 3 times the value of ∇_F compared to a C_4 cover, this proportion arising from the ratio of the m values. Other differences between C_3 and C_4 physiologies might also influence the ratio of the ∇_F values. If this were true for all values of FPAR, then the $\nabla_{S,F}$ values for C_3- and C_4-dominated areas would also be related by the same ratio. The results in Tables 4*c* and 4*d* yield a ratio of $\nabla_{S,F}$ values for the C_3- versus C_4-dominated FIFE sites (IFCs 2, 3, and 4 only) of 2.2 to 3.0, depending on the particular SVI used. It therefore seems plausible that the difference between the $\nabla_{S,F}$ values associated with the FIFE flux sites may be largely a function of vegetation physiology and/or management treatment, expressed through the C_3 cover fraction, V_3. This hypothesis is also supported by an inspection of some of the ∇_F trajectories in Figure 9. Some of the flux

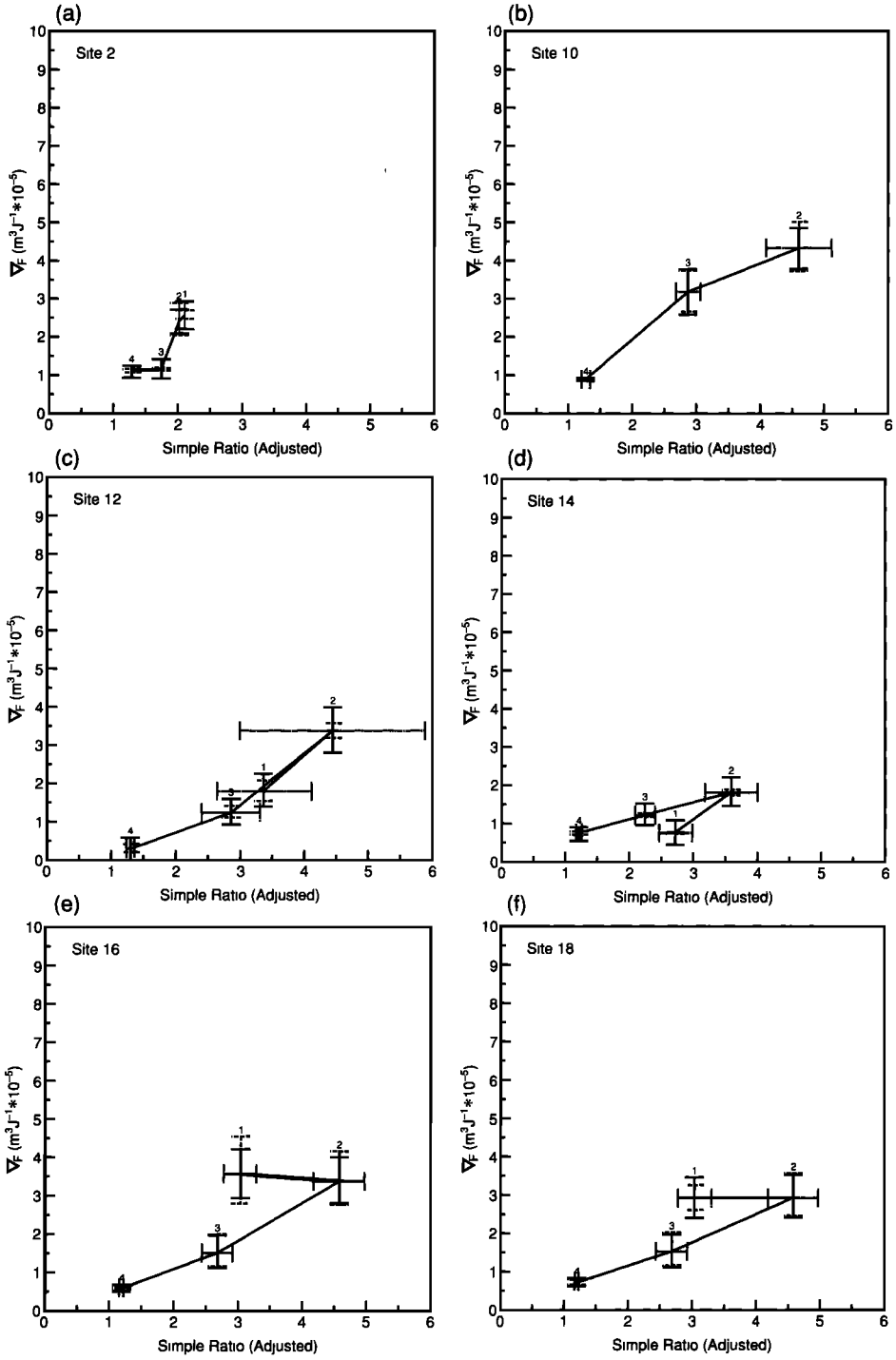

Fig. 9. Derived ∇_F values, from Table 3 and Figure 8, plotted against the radiometrically rectified Landsat thematic mapper (TM) SR vegetation index values acquired closest to the time of the flux observations (see Table 2*b*). SR values are means for a 90 × 90 m area centered on the flux site. Vertical error bars represent the uncertainties due to the soil moisture model (solid bars) and the model goodness of fit (dashed bars) (see text in section 3.4). The horizontal error bars represent the standard deviations of the nine SR values used to compute the mean SR value for each station; see σ_{SR} values in Table 2*b*. The small numbers above the vertical error bars refer to IFCs. (*a*) to (*r*) Individual flux stations. (*s*) All selected (no asterisks in Table 3) flux stations together, uncertainty/error bars excluded for clarity. (*t*) All selected flux stations together; IFCs 2, 3, and 4 only.

stations show a large change in SVI for a relatively small change in ∇_F over the period IFC 1 to IFC 2; see, in particular, stations 16, 18, and 38. This effect is equivalent to a reduction in the site $\nabla_{S,F}$ value which is consistent with the replacement of C_3 (cool season) species in IFC 1 by C_4 (warm season) species in IFC 2 and thereafter (see Table 2*c*).

Figure 10 shows $\nabla_{S,F}$ values for each station plotted against the C_3 cover fraction, V_3, averaged for IFCs 2 and 3. (IFC 4 values of V_3 are considered irrelevant to this part of the analysis as the transpiration fluxes in IFC 4 were very small and thus insensitive to the type of vegetation cover. IFC 1 values of V_3 were not used because of the large C_3 to

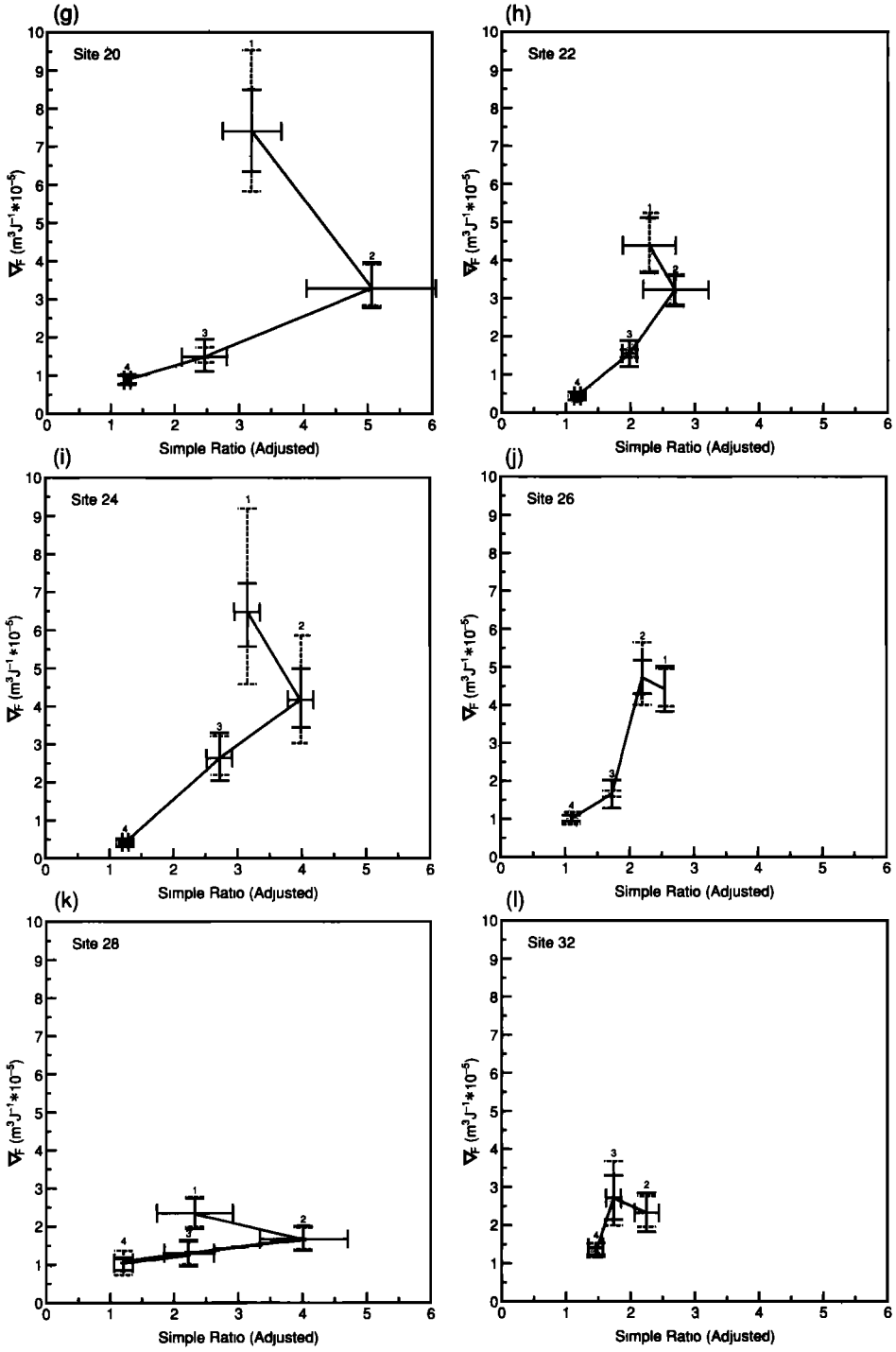

Fig. 9. (continued)

C_4 transitions referred to above.) There is a correlation between the two variables which is consistent with the arguments discussed above: high $\nabla_{S,F}$ values are associated with relatively small FPAR values and high C_3 cover fractions, while the water-efficient C_4 vegetation around some flux stations is associated with the low $\nabla_{S,F}$ values. The scatter in the relationship shown in Figure 10 is hardly surprising, as $\nabla_{S,F}$ is a second-order derivative which can be severely impacted by any noise in the original g_C^* estimates.

In Figure 10 the fit to all the selected station data is shown as a solid line. However, the sites 2 and 12 contributions are suspect. The site 2 data have an anomalous IFC 3 ∇_F value and the area around site 12 had an exceptionally high fraction of woody vegetation (~50% cover), which interfered with the derived value of V_3. If we exclude these two stations, we obtain the dashed line shown in Figure 10 and $r^2 = 0.606$. From the dashed line in Figure 10 we obtain the relationship

$$\nabla_{S,F} = \nabla_{C,S,F} V_3 + a_3 \tag{23}$$

where

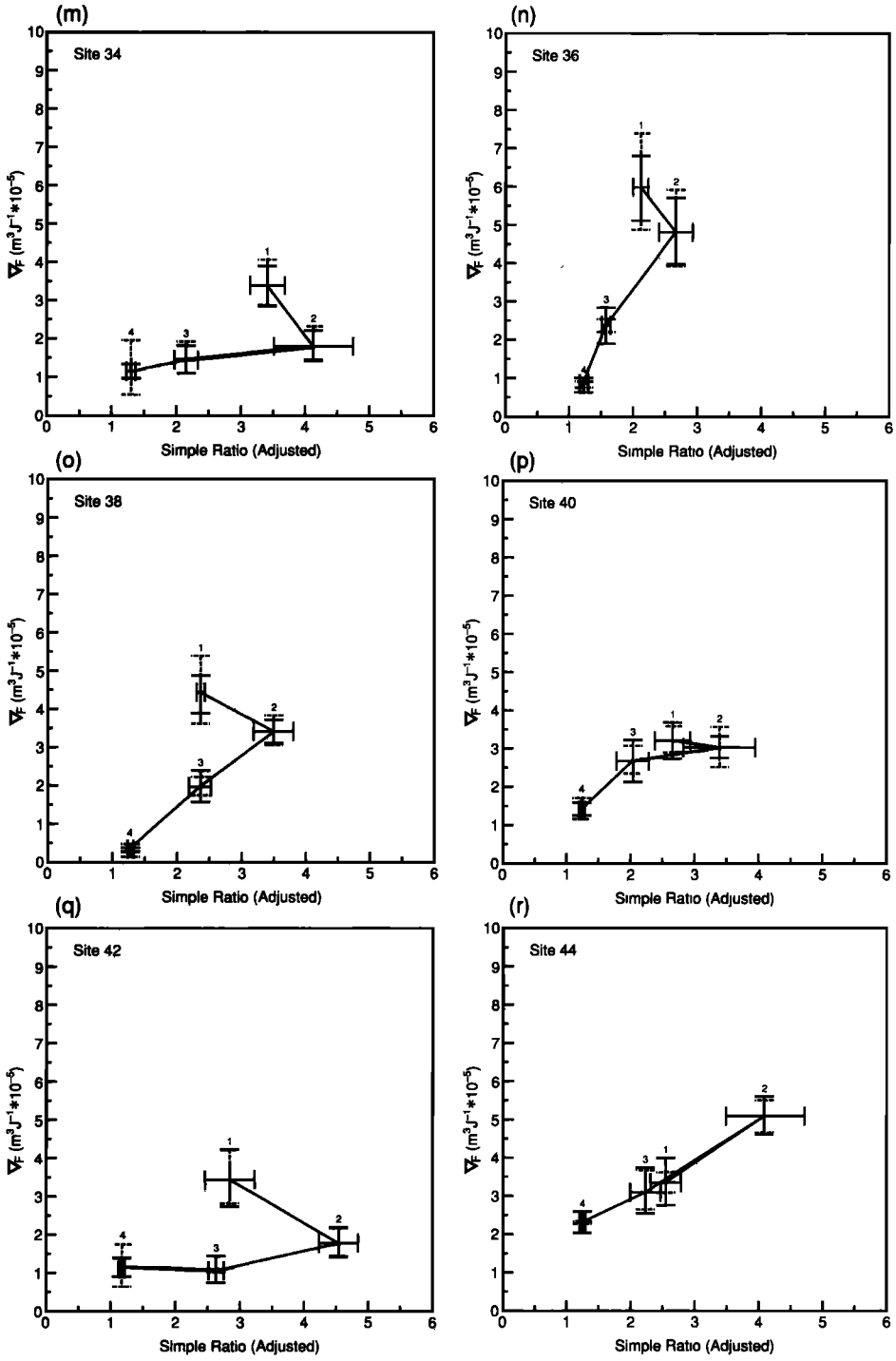

Fig. 9. (continued)

$$\nabla_{C,S,F} \equiv \frac{\partial}{\partial V_3}\left(\frac{\partial}{\partial(\mathrm{SR})}\left(\frac{\partial g_c^*}{\partial F_0}\right)\right) \equiv \frac{\partial}{\partial V_3}\frac{\partial \nabla_F}{\partial(\mathrm{SR})} \equiv \frac{\partial \nabla_{S,F}}{\partial V_3}$$

$\nabla_{C,S,F}$ = slope of dashed line in Figure 10;
$\nabla_{C,S,F} = 5.668 \times 10^{-5}$ m^3 J^{-1} ($r^2 = 0.606$);
V_3 = C_3 cover fraction;
a_3 = intercept of line in Figure 10;
$a_3 = -0.886 \times 10^{-5}$ m^3 J^{-1}.

The dashed line in Figure 10 will be used as the basis for the biophysical model discussed in section 5. However, it is clear that the extrapolation of this line could not be considered a realistic representation of the dependence of $\nabla_{S,F}$ on V_3. From (22) and the knowledge that $m \simeq 9$ for C_3 vegetation and $m \simeq 4$ for C_4 vegetation, the value of $\nabla_{S,F}$ when $V_3 = 1$ must be roughly 2 to 3 times, that is, approximately 9/4, the value of $\nabla_{S,F}$ when $V_3 = 0$. A dotted curve is sketched into Figure 10 showing how the complete relationship might look given these assumptions and the data points. However, the results presented here only justify the use of the linear relationship represented by the dashed line and (23).

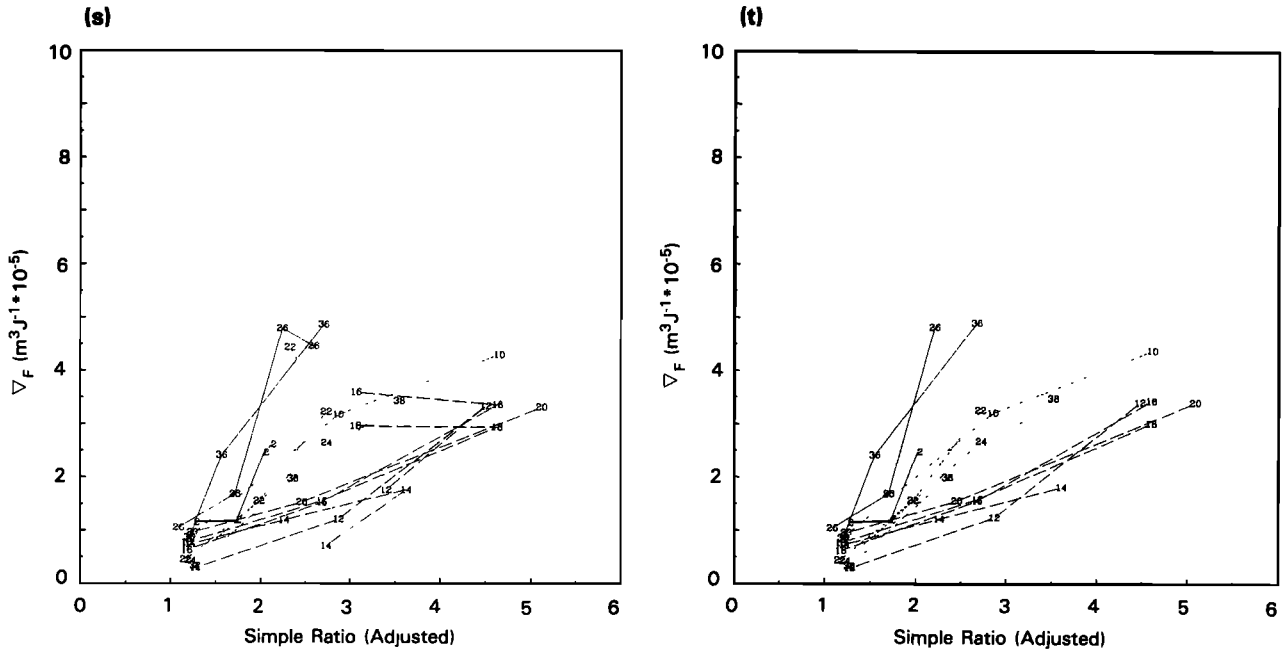

Fig. 9. (continued)

5. Application of a Biophysical Model of Evapotranspiration With Parameters Taken From Spectral Data

5.1. *The Biophysical Model*

From the analyses described in previous sections, we can formulate a biophysical model to describe the unstressed canopy conductance (g_C^*) as a function of incident PAR (F_0), SR vegetation index, as obtained from Landsat TM data, and the C_3 cover fraction (V_3). From Table 4 and Figure 10 we have

$$g_C^* = \nabla_F F_0, \tag{24a}$$

$$\nabla_F = \nabla_{S,F}(\mathrm{SR} - a_1) + a_2, \tag{24b}$$

$$\nabla_{S,F} = \nabla_{C,S,F}(V_3) + a_3, \tag{24c}$$

where

$\nabla_F = \partial g_c^*/\partial F_0$, $m^3\ J^{-1}$;
$\nabla_{S,F} = \partial \nabla_F/\partial(\mathrm{SR})$, $m^3\ J^{-1}$;
$\nabla_{C,S,F} = \partial \nabla_{S,F}/\partial(V_3)$, $m^3\ J^{-1}$;
$\nabla_{C,S,F} = 5.668 \times 10^{-5}$;
a_1, a_2 = coordinates of "pivot" point in Table 4*c*;
a_1, a_2 = 0.774, 0.0;
a_3 = intercept in Figure 10;
$a_3 = -0.886 \times 10^{-5}\ m^3\ J^{-1}$.

Figure 11 shows a schematic summary of (24). The next few sections discuss applications and tests of this model. Figure 12 shows the different scales addressed in the analysis: the flux station scale (90 × 90 km), the airborne eddy correlation scale (2 × 4 km), and the scale of the entire site (15 × 15 km).

5.2. *Local-Scale (Flux Station) Application of the Conductance Model*

Equation (24) was applied at the local scale using data associated with individual flux stations for days 227 and 280 in FIFE 87 and days 209 and 216 for FIFE 89 (see bottom panel of Figure 12). It should be noted that the FIFE 89 data, see Table 2, were not used in any of the analyses which resulted in the formulation of (24) so their use can be considered as a blind test of the model. A mean value of $\nabla_{S,F} = 1.394 \times 10^{-5}$ was used throughout, as no detailed information on V_3 was available for FIFE 89; this test therefore represents an application of (24*a*) and (24*b*) only.

The model was provided with the values of SR for each site listed in Table 2 and initialized and forced with meteorological and soil data, as discussed in section 3. Time series of the calculated fluxes for each day were averaged over the hours specified at the top of Figure 13; these time periods correspond to the times when the Twin Otter aircraft (eddy correlation; ABL-6) was operating over the site. These means are compared with the means of the observed fluxes for each station and are plotted against each other as circles in Figure 13. Several points are apparent from these results.

1. Overall, the simulations reproduce the range of observed fluxes fairly well, see especially the summary figures ("all days-surface stations").

2. For each day the flux station observations of available energy, $R_n - G$ (or $\lambda E + H$ for the eddy correlation stations), show a wider range than the SiB calculations. There are two reasons for this: first, the SiB calculations made no allowance for site slope and aspect; second, the forcing downward radiation fluxes were assumed to be uniform over the site in all of the model runs.

3. The day 227 SiB calculations of latent heat flux are higher than the observations. Day 227 immediately followed two days of heavy rainfall and the soil surface was very moist, wetter than any of the test cases used to develop the r_{surf} formulation of (19). We suspect that the soil evaporation component has been overestimated by the equation (19) model for this day.

4. The two FIFE 89 days, 209 and 216, made use of the same SR data but different soil moisture initializations. The model reproduces the range of fluxes for each day and also

TABLE 4a. Calculated Slopes, ($\nabla_{S,F}$), Intercepts (SR or ND Intercept), and Standard Deviations ($\sigma\nabla_F$) of ∇_F Versus SVI Values, Obtained by Best Fits to the IFCs 2, 3, and 4 Results Shown in Figure 9t

Site	$\nabla_{S,F}$	$SR_{intercept}$	$\nabla_{F_{intercept}}$	$\sigma\nabla_F$
2	1.583	0.680	−1.076	0.429
10	1.018	0.159	−0.162	0.366
12	0.969	1.186	−1.149	0.341
14	0.448	−0.407	0.182	0.005
16	0.825	0.580	−0.479	0.172
18	0.658	0.135	−0.089	0.098
20	0.643	−0.101	0.065	0.099
22	1.801	0.996	−1.793	0.200
24	1.489	0.952	−1.418	0.000
26	3.237	0.908	−2.940	0.820
36	2.603	0.785	−2.043	0.325
38	1.394	1.015	−1.414	0.084
C_3	2.684	0.886	−2.377	0.694
C_4	0.734	0.461	−0.338	0.294

Unconstrained fits to individual flux station data: ∇_F versus SR. $\nabla_{S,F}$, $\nabla_{F\text{intercept}}$, and $\sigma\nabla_F$ are in units of $m^3\ J^{-1} \times 10^{-5}$.

the changes in the fluxes from 209 to 216 following the rainstorms of days 212–215.

5.3. *Intermediate-Scale (Airborne Eddy Correlation) Application of the Conductance Model*

The middle panel of Figure 12 shows the arrangement of 2 × 4 km areas over the FIFE area which were assigned time-averaged flux estimates by *Desjardins et al.* [1990], based on their low-level airborne eddy correlation observations. The SiB calculations made use of interpolated soil moisture fields, based on soil moisture observations made at the flux stations, which were contoured and integrated to provide mean estimates of W_1, W_2, and W_3 for the 2 × 4 km areas. The SR images were also analyzed to provide similar mean values for each area. The meteorological forcings for the four days were provided by the spatial means of the automatic weather station data which were applied as time series values of T_r, e_r, u_r, $S\downarrow$, and $L\downarrow$, with a time step of 30 min, as in all other cases in this paper. The resulting calculated fluxes were time averaged and compared to the observations of *Desjardins et al.* [1990] in Figure 13 (small crosses) and as fields in Plate 1. From Figure 13 it is immediately obvious that the observed energy fluxes are systematically lower, between 15 and 30%, than the calculated ones. Given that no such trend exists between the surface flux station observations and the SiB calculations, see previous section, it is reasonable to assume that the airborne eddy correlation fluxes reproduced here are underestimates, for the reasons discussed at length in papers in the Atmospheric Boundary Layer section of this issue. However, as reported elsewhere, the underestimation seems well behaved and may approximate to a constant proportion of the sensible and latent heat fluxes. In any case, the evaporative fractions calculated by the model compare well with the observations, see Figures 13 and Plate 1. The relatively "flat" fields of evaporative fraction observed and calculated for days 227 and 280 in FIFE 87 correspond to the relatively uniform SR fields for those days, see Plate 1. However, in FIFE 89, nonuniform rainfall gave rise to the so-called "green finger" SR anomaly which translates into anomalies in the observed and calculated evaporative fraction fields.

TABLE 4c. Constrained (Single Pivot-Point) Best Fits: ∇_F Versus SR

Site	$\nabla_{S,F}$	$SR_{intercept}$	$\nabla_{F_{intercept}}$	$\sigma\nabla_F$
2	1.727	0.774	−1.337	0.433
10	1.226	0.774	−0.949	0.555
12	0.831	0.774	−0.643	0.426
14	0.690	0.774	−0.534	0.338
16	0.879	0.774	−0.680	0.204
18	0.799	0.774	−0.619	0.305
20	0.812	0.774	−0.628	0.422
22	1.538	0.774	−1.190	0.303
24	1.330	0.774	−1.030	0.196
26	2.848	0.774	−2.205	0.854
36	2.580	0.774	−1.997	0.325
38	1.237	0.774	−0.958	0.218
C_3	2.440	0.774	−1.889	0.709
C_4	0.812	0.774	−0.629	0.323

5.4. *Application of the Conductance Model on the Scale of the FIFE Area*

Sellers et al. [1992] present arguments which suggest that area-averaged SVI values should provide reasonable estimates of the area integrals of land surface photosynthesis and conductance: a key assumption in their analysis was that under certain conditions, SVI should be near-linearly related

TABLE 4b. Unconstrained Fits to Individual Flux Station Data: ∇_F Versus ND

Site	$\nabla_{S,F}$	$ND_{intercept}$	$\nabla_{F_{intercept}}$	$\sigma\nabla_F$
2	5.058	−0.070	0.353	0.472
10	6.332	−0.032	0.200	0.068
12	5.562	0.112	−0.625	0.708
14	2.250	−0.201	0.452	0.104
16	4.652	−0.003	0.012	0.524
18	3.748	−0.077	0.289	0.379
20	4.274	−0.059	0.253	0.431
22	7.049	0.043	−0.300	0.416
24	6.217	0.038	−0.236	0.000
26	10.075	−0.017	0.170	1.020
36	11.060	0.014	−0.151	0.096
38	7.039	0.090	−0.633	0.208
C_3	9.625	0.009	−0.089	0.807
C_4	4.211	−0.012	0.052	0.497

TABLE 4d. Constrained (Single Pivot-Point) Best Fits: ∇_F Versus ND

Site	$\nabla_{S,F}$	$ND_{intercept}$	$\nabla_{F_{intercept}}$	$\sigma\nabla_F$
2	6.351	0.003	−0.017	0.498
10	6.728	0.003	−0.018	0.147
12	4.395	0.003	−0.012	0.786
14	3.244	0.003	−0.009	0.288
16	4.702	0.003	−0.013	0.524
18	4.303	0.003	−0.011	0.422
20	4.770	0.003	−0.013	0.461
22	6.316	0.003	−0.017	0.447
24	5.686	0.003	−0.015	0.166
26	10.729	0.003	−0.029	1.028
36	10.729	0.003	−0.029	0.122
38	5.704	0.003	−0.015	0.395
C_3	9.425	0.003	−0.025	0.808
C_4	4.352	0.003	−0.012	0.498

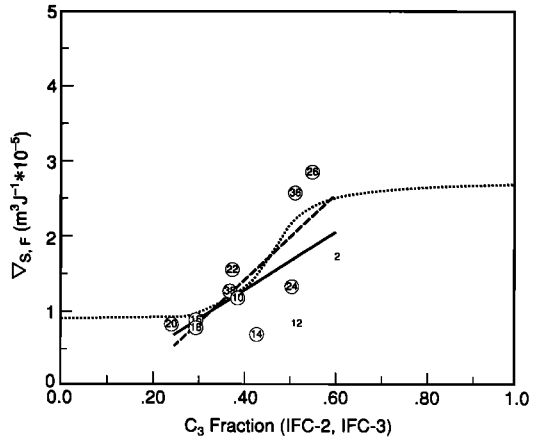

Fig. 10. Values of $\nabla_{S,F}$ (slope of ∇_F versus SR) plotted against C_3 cover fraction, V_3. The $\nabla_{S,F}$ values were obtained by best fits to ∇_F and SR values, see Table 4c. V_3 values are means from IFCs 2 and 3 staff science survey data. Solid line shows fit to all data (r^2 = 0.384); dashed line shows fit to circled stations (r^2 = 0.606); dotted curve shows hypothesized relationship for all values of V_3.

to ∇_F, a condition which appears to be satisfied for the FIFE site, see Figure 9. We can build on these arguments to calculate a single-area-averaged value of ∇_F for the FIFE site for any given TM image based on the simple combination of the site-averaged values of SR and V_3, see Figure 12.

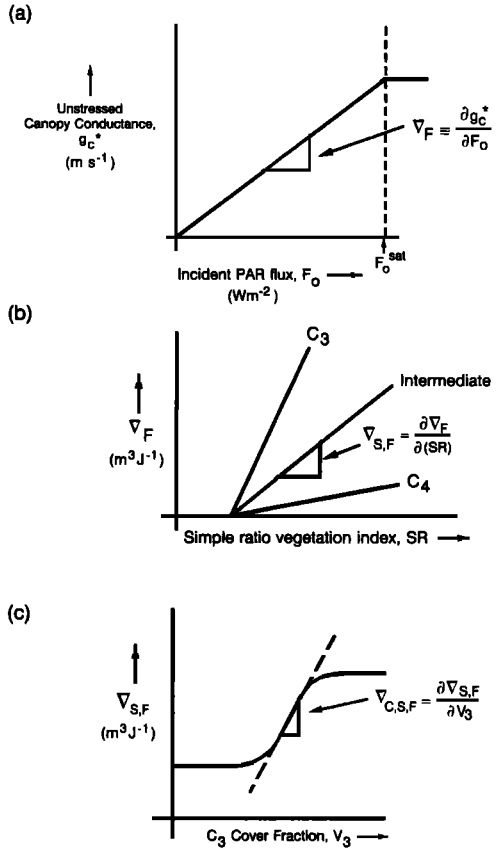

Fig. 11. Schematic summary of (24). (*a*) Equation (24*a*): relationship between g_C^* and F_0; slope is ∇_F. (*b*) Equation (24*b*): relationship between ∇_F and SR; slope is $\nabla_{S,F}$. (*c*) Equation (24*c*): relationship between $\nabla_{S,F}$ and V_3; slope is $\nabla_{C,S,F} = 5.668 \times 10^{-5}$ m^3 J^{-1} over the center portion (dashed line) of the curve.

It should be remembered that although the SR:∇_F relationship appears to be almost linear, the relationship between the ∇_F and the energy fluxes is somewhat nonlinear due to the effects of the stress factors, $f(x_i)$, and the aerodynamic resistances. We might expect therefore that the relationship between the calculated energy fluxes and SR to be more or less scale-dependent.

For this calculation, site-averaged initial values of W_1, W_2, and W_3 were specified and the spatial mean meteorological forcing was applied as before. The resulting site scale fluxes are compared to the site-scale aggregates of the *Desjardins et al.* [1990] observations in Figure 13 (large crosses); the same trends and biases reported for the 2 × 4 km scale studies reported in the previous section are apparent here.

A more rigorous test of the scale invariance of the model's performance was conducted. The FIFE area was divided into 1 × 1 km subareas and each was assigned SR and initial soil moisture values in the same way as was done for the 2 × 4 km areas, as described in section 5.3. Each 1 × 1 km area was then forced with the spatial mean meteorological forcings for the few days shown in Figures 13 and Plate 1 and the results combined to produce an estimate of the area mean flux and its standard deviation, displayed as time series in Figure 14. Also shown are the results obtained using a single-site-averaged value of ∇_F derived from the site-mean value of SR and the site-averaged values of W_1, W_2, and W_3. Even though the range of fluxes reproduced by the aggregated cases is sometimes very large, as in the FIFE 89 cases, the area-averaged values do not differ by more than

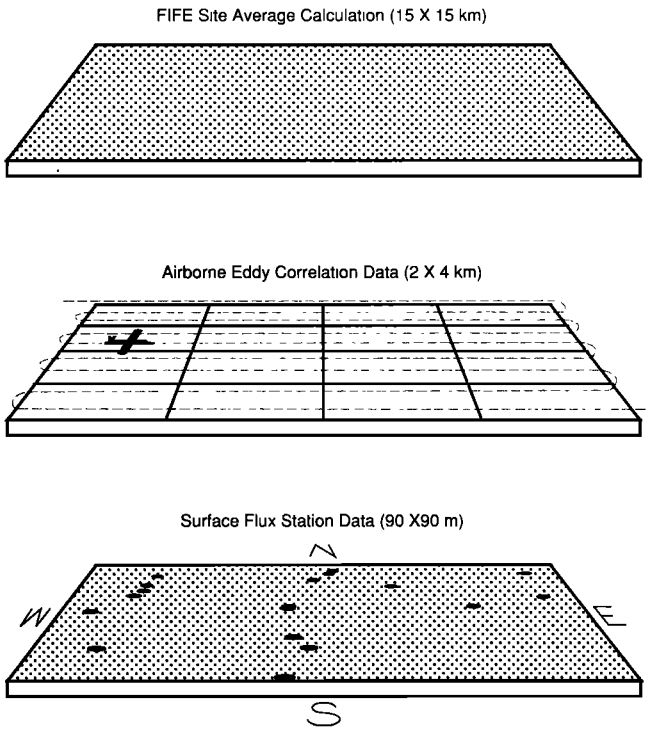

Fig. 12. Schematic of the range of spatial scales addressed in this paper. (Bottom) Array of surface flux stations for FIFE 87. SR values averaged for 90 × 90 m areas centered on each site were taken to be representative of the vegetation cover. (Middle) Pattern of 2 × 4 km boxes used for representing the airborne eddy correlation analyses of *Desjardins et al.* [1990]. (Top) Scale of entire FIFE site. A site-averaged value of SR was used to represent the average vegetation condition.

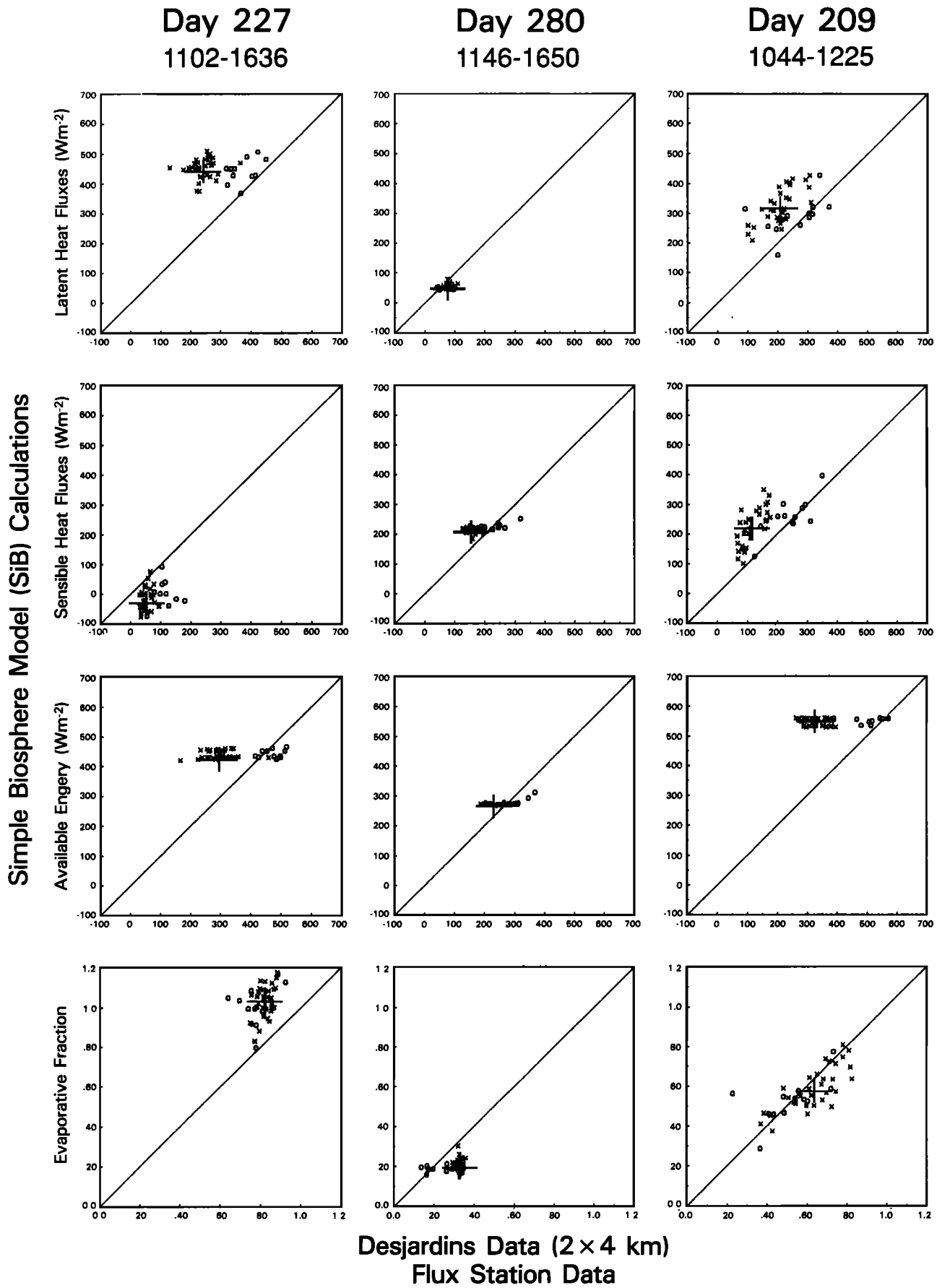

Fig. 13. Comparison of SiB calculations of latent heat flux (λE), sensible heat flux (H), available energy ($R_n - G = H + \lambda E$), and evaporative fraction ($\lambda E/(H + \lambda E)$) with surface flux station observations (circles); and the analyses of airborne eddy correlation data, as reported by *Desjardins et al.* [1990] (small crosses). The values shown are time means for the periods specified at the top of the figures for the FIFE 87, days 227 and 280 and for the FIFE 89, days 209 and 216. The large crosses represent comparisons between site-average SiB calculations and the site averages of the *Desjardins et al.* [1990] observations.

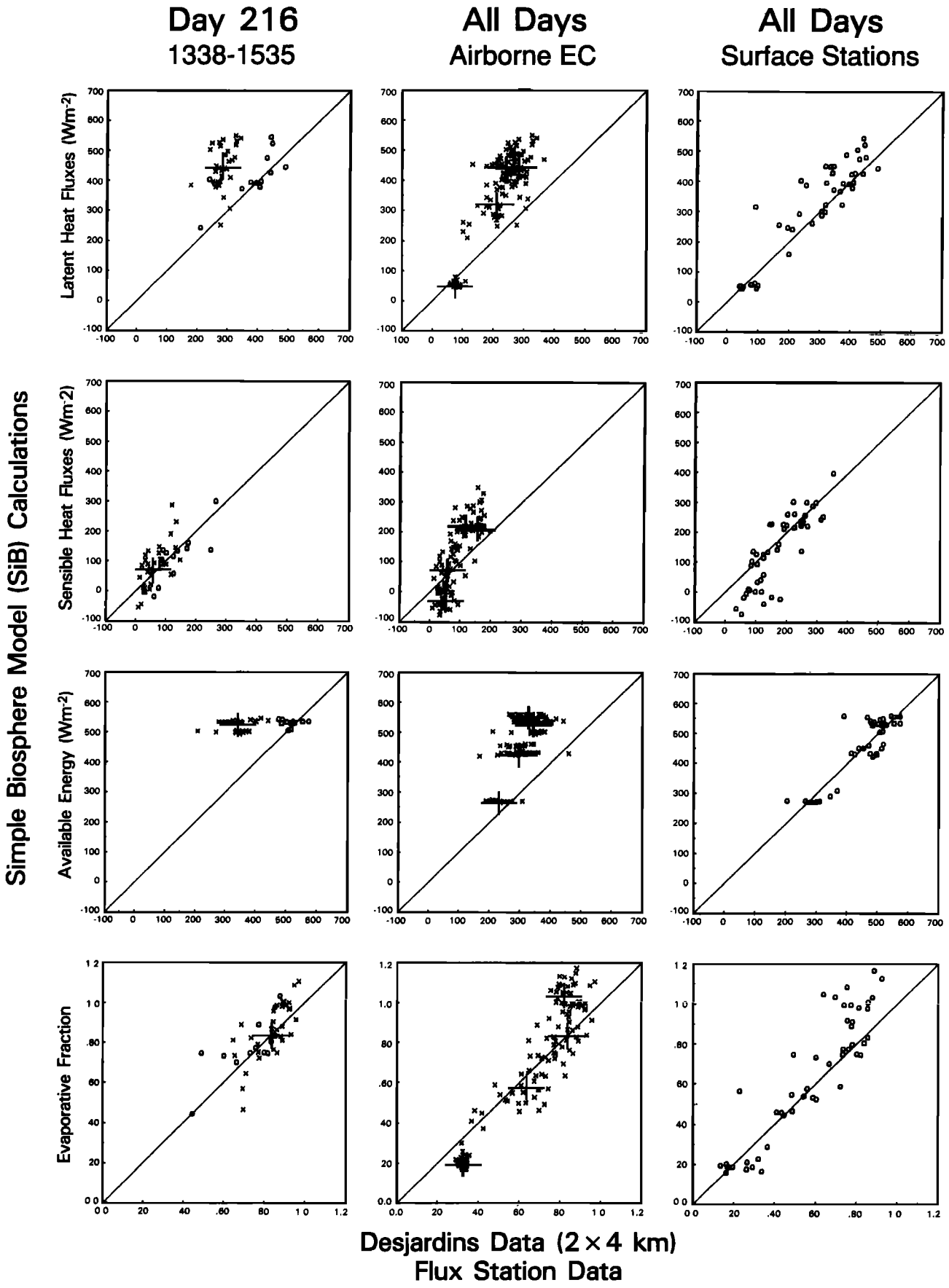

Fig. 13. (continued)

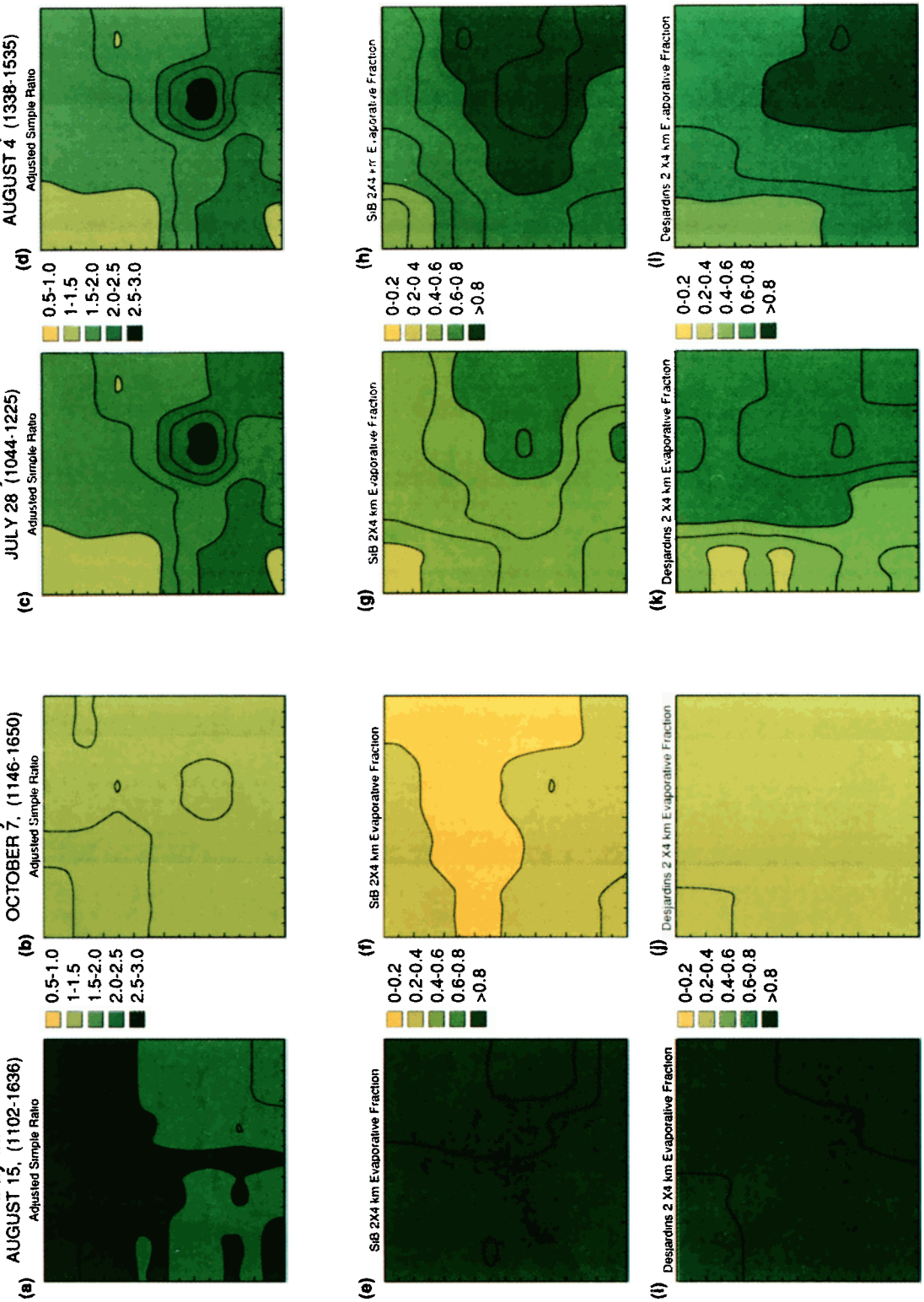

Plate 1. Contour maps of observed and calculated biophysical fields for the entire FIFE site (15 × 15 km) based on analyses conducted using a 2 × 4 km grid. (*a*) to (*d*) Radiometrically rectified Landsat SR data aggregated to 2 × 4 km and contoured. (*e*) to (*h*) Mean calculated evaporative fraction fields, using the SiB model and (24) in text. (*i*) to (*l*) Mean observed evaporative fraction fields, as reported by *Desjardins et al.* [1990]. The results shown in (*e*) to (*l*) are also shown as point values in Figure 13. In this figure they were used as inputs for a computer contouring procedure.

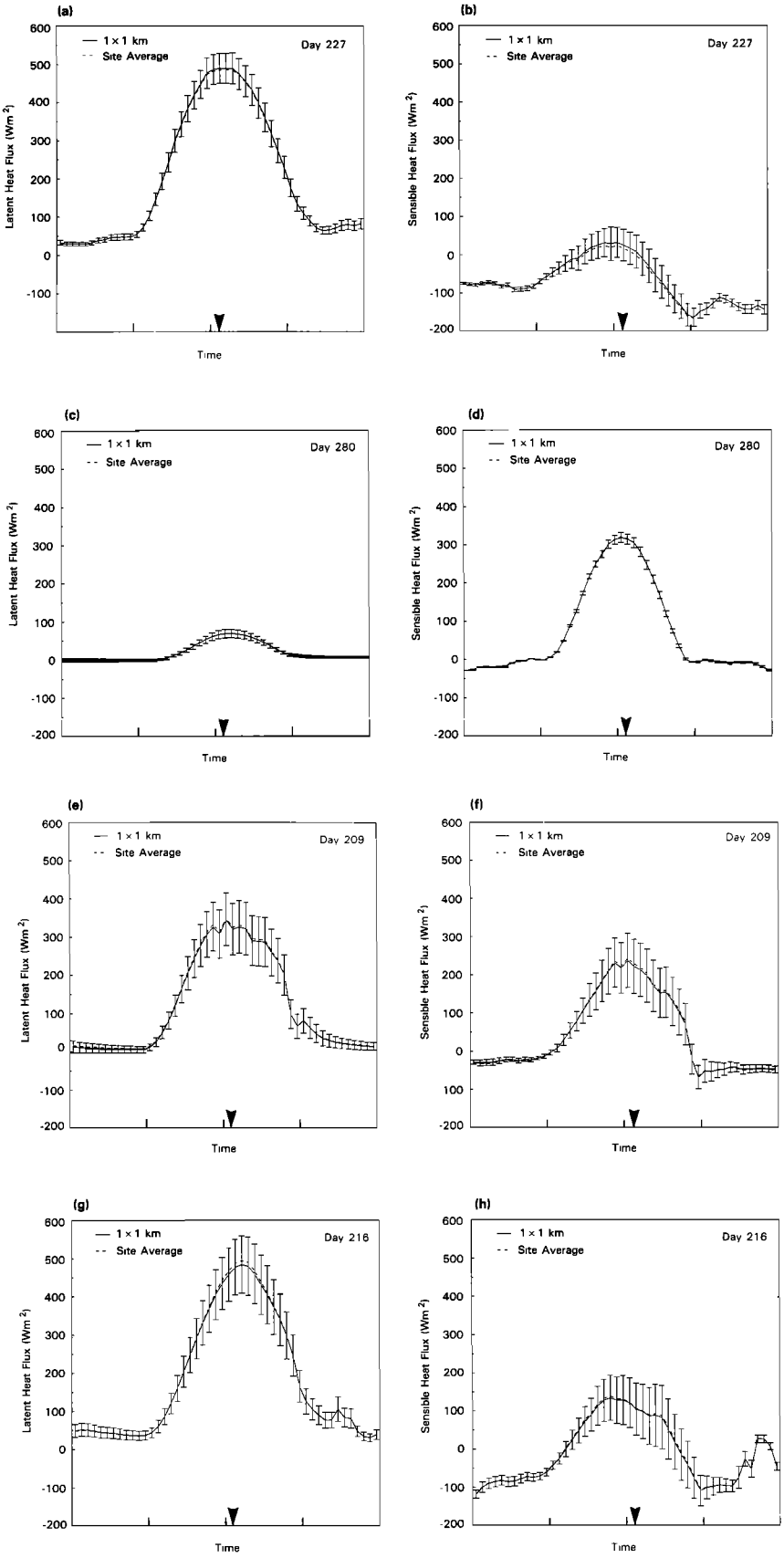

Fig. 14. The effects of scale on the calculation of site-averaged heat fluxes. In each case, the dashed line refers to the site-averaged value obtained using single-site-averaged spatial mean values of SR, ∇_F, and soil moisture. The solid line and error bars refer to the site mean and standard deviation obtained by aggregating separate calculations performed on a 1 × 1 km grid over the site. (*a*) and (*b*) Latent and sensible heat fluxes for day 227, FIFE 87. (*c*) and (*d*) Latent and sensible heat fluxes for day 280, FIFE 87. (*e*) and (*f*) Latent and sensible heat fluxes for day 209, FIFE 89. (*g*) and (*h*) Latent and sensible heat fluxes for day 216, FIFE 89.

3% for any time period. This result is very encouraging with regard to the utility of coarse resolution satellite data for the accurate calculation of energy fluxes over large areas. It should be remembered, however, that the surface soil moisture field must also be specified at the same scale.

6. Summary

The relationship between surface conductance (g_C) and spectral vegetation indices (SVI) was explored using the FIFE data set, principally the surface flux station data and images from the Landsat thematic mapper instrument. It was found that:

1. The unstressed canopy conductance, g_C^*, for a given site for a given day was near-linearly related to the incident PAR flux, F_0 (see Figures 1 and 2*d*). Estimates of g_C^* were obtained via a model inversion which separated the soil and vegetation contributions to evapotranspiration and made adjustments for the effects of vapor pressure deficit and soil moisture stress. This result can be summarized as (equation (24*a*))

$$g_C^* = \nabla_F F_0,$$

or

$$\nabla_F \equiv \frac{\partial g_C^*}{\partial F_0} = \text{constant for a given site and day.}$$

2. For individual flux stations a near-linear relationship existed between the ∇_F and the SR vegetation index, calculated for an area of 90 × 90 m centered on the flux site (equation (24*b*)), see Figure 9.

$$\nabla_F = \nabla_{S,F}(\text{SR} - a_1) + a_2,$$

or

$$\nabla_{S,F} \equiv \frac{\partial \nabla_F}{\partial(\text{SR})} = \text{constant},$$

for a given site over a period when V_3 was constant. V_3 is the percentage cover of C_3 vegetation and a_1 and a_2 are constants.

The above two results concur with the analyses of *Sellers et al.* [1992] which indicate that vegetation canopies allocate photosynthetic machinery in an optimal fashion and so maintain a near-linear relationship between the ∇_F and the fraction of PAR absorbed by the canopy (FPAR). FPAR is in turn near-linearly related to SR [see *Sellers*, 1987] which completes the chain of relationships leading to point 2 above.

3. The slope of the ∇_F versus SR relationship varied from station to station. This variation appeared to be correlated with management treatment and the proportional coverage of C_3 versus C_4 vegetation in the area surrounding the flux station (equation (24*c*)).

$$\nabla_{S,F} = \nabla_{C,S,F}(V_3) + a_3,$$

where

$$\nabla_{C,S,F} \equiv \frac{\partial \nabla_{S,F}}{\partial(V_3)} \simeq \text{constant} = 5.668 \times 10^{-5}\ \text{m}^3\ \text{J}^{-1},\ r^2 = 0.606,$$

where a_3 is a constant and, in this case, V_3 is the percentage cover of C_3 species averaged for IFCs 2 and 3. This result follows from the high stomatal conductances of C_3 species compared to C_4 species.

The above equations were calibrated with the FIFE 87 flux station data to provide a model of canopy conductance which can be driven by remotely sensed data (SR) and some knowledge of the C_3/C_4 cover fraction, see (24) and Figure 11.

The model was used to generate time series and fields of the surface energy balance components on the scale of (1) the surface flux stations (90 × 90 m), (2) the airborne eddy correlation analyses (2 × 4 km), and (3) the entire FIFE site (15 × 15 km).

In all cases the model appeared to produce results that compare well with the surface and airborne flux measurements. More importantly, the model performance proved to be almost scale-invariant which implies that coarse resolution satellite and meteorological data can be used to calculate fields of the surface energy fluxes. This scale invariance is the result of the linear nature of the biophysical model described in this paper and is supported by the theoretical analyses of *Sellers et al.* [1992]. However, it should be noted that some knowledge of the surface soil moisture field is also required to complete these calculations.

Appendix: Estimation of Leaf Area Index Values, Greenness Fractions, and Litter Leaf Area Indexes

In the SiB model, the canopy leaf area index, greenness fraction, and the litter layer (dead vegetation) leaf area index must be specified for the calculation of the radiation budget terms (absorbed shortwave and net radiation). The University of Nebraska teams (SF-6 and SRB-2) made destructive samples of leaf area index at site 16 (4439-ECV) throughout the growing season, and these data were used in conjunction with the site 16 SR values shown in Table 2*b* to formulate a regression relationship for green leaf area index, see *Hall et al.* [1990], which was then used to calculate green leaf area indexes for all the flux stations, see Table 1*b*. KSU staff science members collected green leaf weight, dead leaf weight, and litter weight data for all sites throughout FIFE 87. The dry green and dry leaf weights were ratioed to provide estimates of canopy greenness fractions which were then used to divide the green leaf area index values in Table 1*b* to yield estimates of total canopy leaf area index, see Table 1*b*. The mean ratio of the measured total dry green canopy leaf weight to the derived canopy green leaf area index was used to convert the litter weights to equivalent litter layer leaf area indexes, see Table 1*b*. The canopy and litter layer leaf area indexes and the canopy greenness fraction values were used in the radiation module of SiB to calculate radiative transfer properties of the vegetated surface (canopy reflectance and transmittance, ground reflectance) and the amount of shortwave radiation absorbed by the canopy and ground. The values in Table 1*b* were not used for any other purpose in the analysis discussed in this paper, particularly not for the calculation of ∇_F values described in later sections. It should also be noted that the surface albedo calculation is relatively insensitive to large errors in leaf area index, see *Sellers* [1985, 1987].

Acknowledgments. Piers Sellers and Mark Heiser (IS-4) were supported by a NASA grant throughout this work (NAG5-892). The

support of the Center for Ocean-Land-Atmosphere Interactions (COLA) and the Department of Meteorology at the University of Maryland, NASA Goddard Space Flight Center, and NASA HQ is also gratefully acknowledged. The entire FIFE team contributed to this work in one way or another. The measurements of the surface flux team, the atmospheric boundary layer team, and the continuing support of the FIFE Information System staff (Don Strebel, Fred Huemmrich, Diana Van Elberg-Obler, Jaime Nickerson, Scott Goetz, Dave Landis, and Jeff Newcomer) deserve special mention. The Carnegie/Stanford group (Joe Berry, Chris Field, Jim Collatz, and others) also provided useful input at a critical point in the analysis. Marlene Schlichtig typed and edited the entire paper. This paper is dedicated to the memory of Peter Camillo who was liked and admired by all who knew him in the FIFE team. He is missed.

REFERENCES

Asrar, G., M. Fuchs, E. T. Kanemasu, and J. L. Hatfield, Estimating absorbed photosynthetic radiation and leaf area index from spectral reflectance in wheat, *Agron. J.*, *76*, 300, 1984.

Ball, J. T., An analysis of stomatal conductance, Ph.D. thesis, 89 pp., Stanford Univ., Stanford, Calif., 1988.

Camillo, P. J., and R. J. Gurney, A resistance parameter for bare soil evaporation models, *Soil Sci.*, *141*(2), 94–105, 1986.

Choudhury, B. J., Relationships between vegetation indices, radiation absorption and net photosynthesis evaluated by a sensitivity analysis, *Remote Sens. Environ.*, *22*, 209–234, 1987.

Clapp, R. B., and G. M. Hornberger, Empirical equations for some soil hydraulic properties, *Water Resour. Res.*, *14*(4), 601–604, 1978.

Collatz, G. J., J. T. Ball, C. Grivet, and J. A. Berry, Physiological and environmental regulation of stomatal conductance, photosynthesis and transpiration: A model that includes a laminar boundary layer, *Agric. For. Meteorol.*, *54*, 107–136, 1991.

Desjardins, R. L., P. H. Schuepp, and J. I. MacPherson, Spatial and temporal variations of CO_2, sensible and latent heat fluxes over the FIFE site, in *Proceedings of the AMS FIFE Symposium*, pp. 46–50, American Meteorological Society, Boston, Mass., 1990.

Farquhar, G. D., S. von Caemmerer, and J. A. Berry, A biochemical model of photosynthetic CO_2 fixation in leaves of C_3 species, *Planta*, *149*, 78–90, 1980.

Field, C. B., and H. A. Mooney, The photosynthesis-nitrogen relationship in wild plants, in *On the Economy of Plant Form and Function*, edited by Thomas J. Givnish, pp. 25–55, Cambridge University Press, New York, 1986.

Goudriaan, J., *Crop Micrometeorology: A Simulation Study*, 249 pp., Wageningen Center for Agricultural Publishing and Documentation, Wageningen, Netherlands, 1977.

Goward, S. N., C. J. Tucker, and D. G. Dye, North American vegetation patterns observed with the NOAA-7 Advanced Very High Resolution Radiometer, *Vegetatio*, *64*, 3–14, 1985.

Hall, F. G., K. F. Huemmrich, and S. N. Goward, Use of narrow-band spectra to estimate the fraction of absorbed photosynthetically active radiation, *Remote Sens. Environ.*, *32*(1), 47–54, 1990.

Hall, F. G., D. E. Strebel, J. E. Nickeson, and S. J. Goetz, Radiometric rectification: Toward a common radiometric response among multidate, multisensor images, *Remote Sens. Environ.*, *35*(1), 11–27, 1991.

Hall, F. G., K. F. Huemmrich, S. J. Goetz, P. J. Sellers, and J. E. Nickerson, Satellite remote sensing of surface energy balance: Success, failures, and unresolved issues in FIFE, *J. Geophys. Res.*, this issue.

Kittel, T. G. F., A. K. Knapp, T. Seastedt, and D. S. Schimel, A landscape view of biomass, LAI and photosynthetic capacity for FIFE, in *Proceedings of the AMS FIFE Symposium*, pp. 66–69, American Meteorological Society, Boston, Mass., 1990.

Monteith, J. L., Climate and the efficiency of crop production in Britain, *Philos. Trans. R. Soc., London, Ser. B*, *281*, 277–294, 1977.

Polley, H. W., J. M. Norman, T. J. Arkebauer, E. A. Walter-Shea, D. H. Greegor, Jr., and B. Bramer, Leaf gas exchange of *Andropogen gerardii* Vitman, *Panicum virgatum* L., and *Sorghastrum nutans* (L.) Nash in a tallgrass prairie, *J. Geophys. Res.*, this issue.

Schimel, D. S., T. G. F. Kittel, A. K. Knapp, T. R. Seastedt, W. J. Parton, and V. B. Brown, Physiological interactions along resource gradients in a tall grass prairie, *Ecology*, *72*(2), 672–684, 1991.

Schuepp, P. H., M. Y. LeClerc, J. I. MacPherson, and R. L. Desjardins, Footprint prediction of scalar fluxes from analytical solutions of the diffusion equation, *Boundary Layer Meteorol.*, *50*, 353–373, 1990.

Sellers, P. J., Canopy reflectance, photosynthesis and transpiration, *Int. J. Remote Sens.*, *6*(8), 1335–1372, 1985.

Sellers, P. J., Canopy reflectance, photosynthesis, and transpiration, II, The role of biophysics in the linearity of their interdependence, *Remote Sens. Environ.*, *21*, 143–183, 1987.

Sellers, P. J., Y. Mintz, Y. C. Sud, and A. Dalcher, A Simple Biosphere Model (SiB) for use within general circulation models, *J. Atmos. Sci.*, *43*, 505–531, 1986.

Sellers, P. J., W. J. Shuttleworth, J. L. Dorman, A. Dalcher, and J. M. Roberts, Calibrating the Simple Biosphere Model (SiB) for Amazonian tropical forest using field and remote sensing data, I, Average calibration with field data, *J. Appl. Meteorol.*, *28*, 727–759, 1989.

Sellers, P. J., J. A. Berry, G. J. Collatz, C. B. Field, and F. G. Hall, Canopy reflectance, photosynthesis and transpiration, III, A reanalysis using improved leaf models and a new canopy integration scheme, *Remote Sens. Environ.*, in press, 1992.

Shu Fen Sun, Moisture and heat transport in a soil layer forced by atmospheric conditions, M.S. thesis, 72 pp., Dep. of Civil Eng., Univ. of Conn., Storrs, 1982.

Shuttleworth, W. J., et al., Eddy correlation measurements of energy partition for Amazonian forest, *Q. J. R. Meteorol. Soc.*, *110*, 1143–1163, 1984*a*.

Shuttleworth, W. J., et al., Observation of radiation exchange above and below Amazonian forest, *Q. J. R. Meteorol. Soc.*, *110*, 1163–1169, 1984*b*.

Stewart, J. B., and S. B. Verma, Comparison of surface fluxes and conductances at two contrasting sites within the FIFE area, *J. Geophys. Res.*, this issue.

Verma, S. B., P. J. Sellers, C. L. Walthall, F. G. Hall, J. Kim, and S. J. Goetz, Photosynthesis and stomatal conductance related to reflectance on the canopy scale (10–100 m)^2, *Remote Sens. Environ.*, in press, 1992.

Villalobos, F. J., and E. Fereres, Evaporation measurements beneath corn, cotton and sunflower canopies, *Agron. J.*, *82*, 1153–1159, 1990.

F. G. Hall and P. J. Sellers, NASA Goddard Space Flight Center, Code 923, Greenbelt, MD 20771.

M. D. Heiser, COLA, Department of Meteorology, University of Maryland, College Park, MD 20740.

(Received August 22, 1991;
revised April 23, 1992;
accepted May 4, 1992.)